

75-106

Génie Electrical Electrique Engineering

Technical Report TR - 76 - 6

2/

ANALYTICAL APPROACH TO THE DESIGN OF
SELECTED MICROWAVE INTEGRATED CIRCUIT
STRUCTURES: *final report*

by

(Wolfgang J.R. Hoefer)

April, 1976

IC

LKC
P
91
.C654
H63
1976



UNIVERSITÉ D'OTTAWA
UNIVERSITY OF OTTAWA

THE UNIVERSITY OF OTTAWA
DEPARTMENT OF ELECTRICAL ENGINEERING
OTTAWA, CANADA

Technical Report TR - 76 - 6

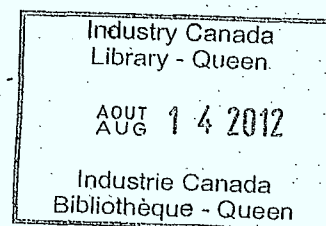
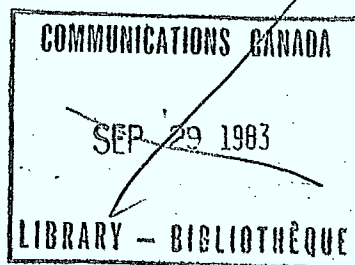
2
ANALYTICAL APPROACH TO THE DESIGN OF
SELECTED MICROWAVE INTEGRATED CIRCUIT
STRUCTURES: *final report*

by

(Wolfgang J.R. Hoefer)

April, 1976

FINAL REPORT TO
Dr. David S. James
C.R.C. Ottawa



D
91
C654
H641
1976

DD 3958505
DL 3966457



FOREWORD

The work described in the present final report was sponsored by the Department of Communications, Communications Research Centre, Ottawa, Canada, under Contract Serial Number OSU5-0026, D.S.S. File Number OLSU. 36100-5-0222.

The analytical work and most of the experimental work was carried out in the Department of Electrical Engineering, University of Ottawa, between March 75 and April 76.

Dr. D.S. James was instrumental in beginning this project and offered valuable advice and help throughout its progress. Graduate students A. Chattopadhyay, M. Cuhaci, K. Masand and G. Painchaud made valuable contributions through experimental work and discussions. Prof. W. Steenaart offered many helpful suggestions and ideas.

This final report summarizes the analysis of selected Microwave Integrated Circuit (MIC) structures and provides formulas for their design. The open microstrip line which is the basic element common to all these structures, is consistently represented by a parallel plate model simple and accurate enough for the analysis of the following selected arrangements: Triangular planar resonators with galvanic, capacitive and hole coupling to microstrip, transitions from microstrip to waveguide and cavities, and some transverse obstacles in microstrip.

Structures were chosen mainly because of their relevance to current projects at the Communications Research Centre in Ottawa. All analytical results (except those on triangular resonators) were experimentally verified and found to be in good agreement with measurements.

After a short description of the selected Microwave Integrated Circuit structures, the methods of analysis are outlined briefly. A description of the experimental techniques and a comparison between theoretical and experimental results conclude the report.

DESCRIPTION OF SELECTED STRUCTURES2.1 THE MICROSTRIP MODEL

All structures discussed in this report include an open microstrip transmission line. Its analytical treatment becomes relatively simple if it is replaced by a parallel plate model with magnetic sidewalls as shown in Fig. 1. The characteristic impedance and the effective dielectric constant of both model and original line are the same for the quasi-TEM mode. However, higher modes of propagation in the model approximate the behaviour of equivalent modes in the original structure to the first order only. Thus, the successful

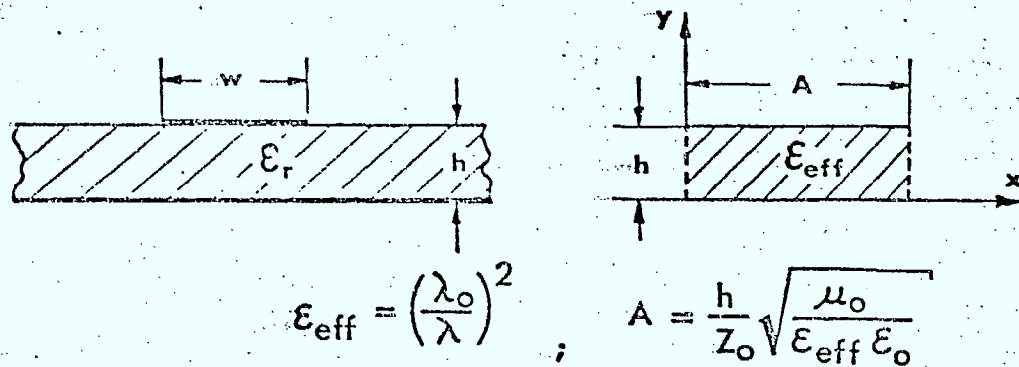


Fig. 1 Microstrip line and its equivalent parallel plate model with magnetic sidewalls.

application of the model is limited to low frequencies, i.e. frequencies below cutoff of higher modes. The main advantage of the parallel plate model resides in the simplicity of the propagating fields and the straightforward boundary conditions it imposes.

2.2 TRIANGULAR PLANAR RESONATORS

Triangular planar resonators are thin metallic equilateral triangular discs deposited on a dielectric substrate which is backed by a conductive ground plane. Such a structure is not only interesting from a theoretical point of view but seems to possess lower radiation losses than circular or rectangular planar resonators of equal resonant frequency.

Fig. 2 shows such a triangular resonator together with a model featuring magnetic sidewalls. As in the case of the microstrip line, this model provides simplified boundary conditions while exhibiting the same resonant frequency and the same stored energy as the original resonator.

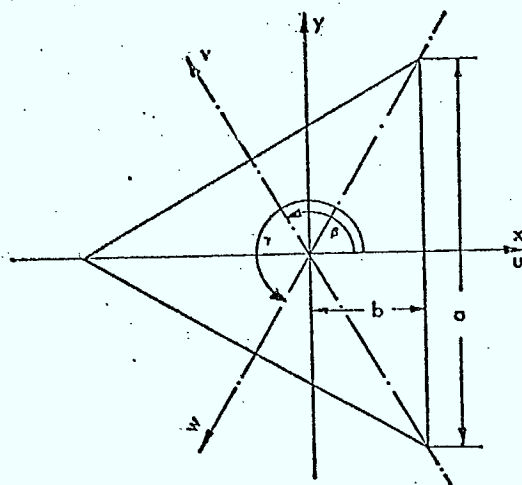


Fig. 2a Shape and dimensions of a planar triangular resonator (top plate)

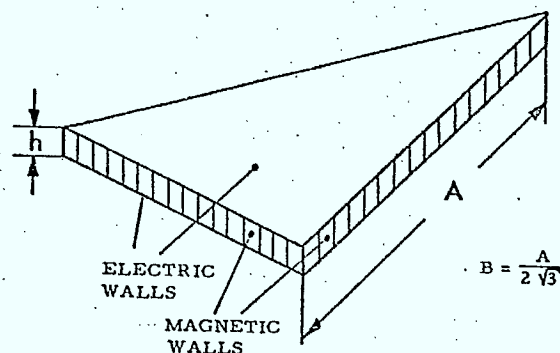


Fig. 2b Model of triangular resonator featuring magnetic side walls.

2.3 COUPLING ARRANGEMENTS AND TRANSITIONS

2.3.1 Coupling between triangular planar resonators and microstrip/waveguide

The following practical methods of coupling between triangular resonators and microstrip/waveguide have been analyzed:

- (a) Direct (galvanic) coupling between a microstrip line and the resonator (Tight coupling)
- (b) Capacitive coupling between a microstrip line and the resonator (Loose coupling)
- (c) Hole coupling between a microstrip line and the resonator through the common ground plane (Loose coupling)
- (d) Hole coupling between a rectangular waveguide and a triangular resonator (Loose coupling).

Fig. 3 shows some typical examples of these coupling arrangements which have been studied.

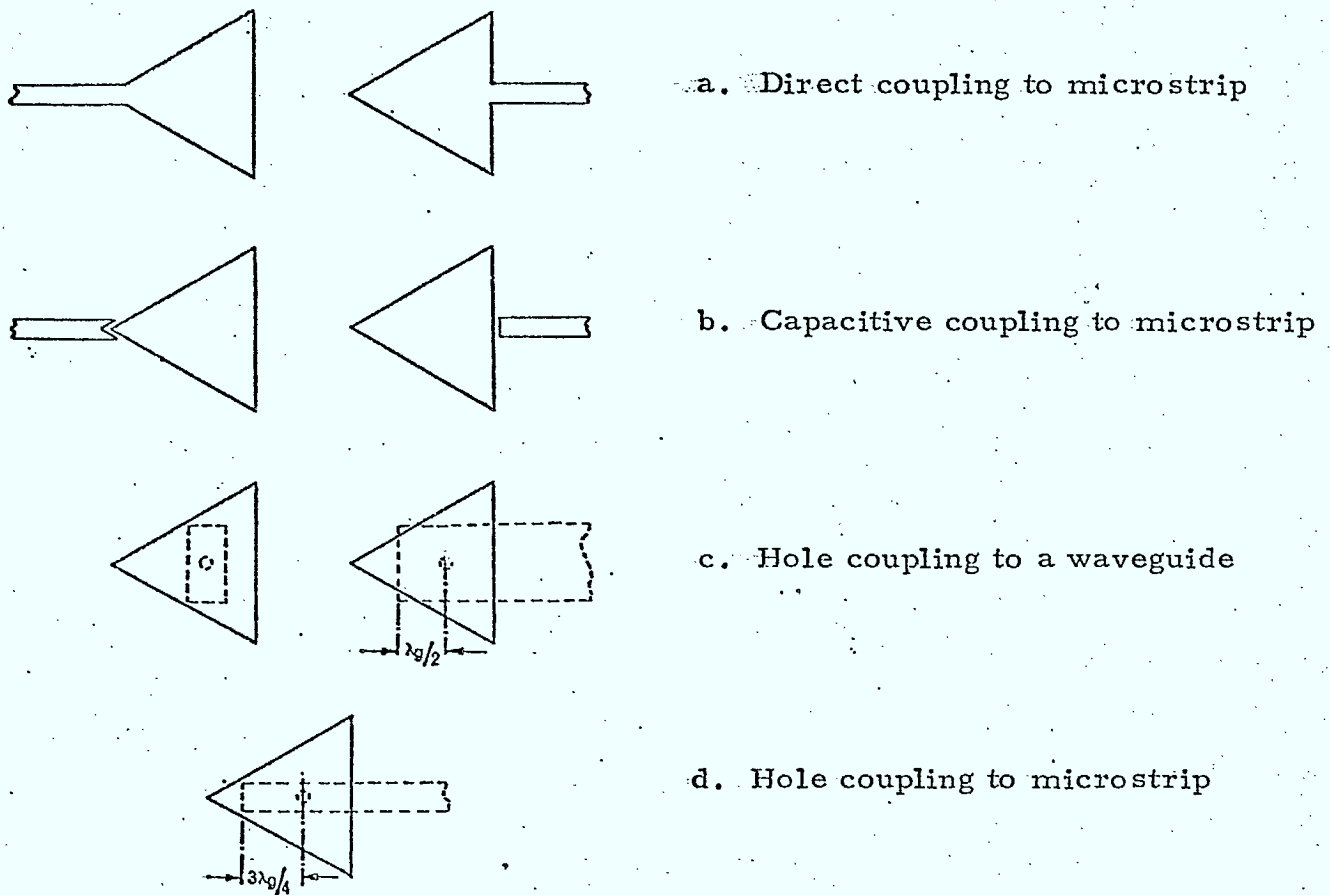


Fig. 3 Some possibilities of coupling between a microstrip/waveguide and a triangular planar resonator which have been studied under the present contract.

The strength of coupling has been evaluated in terms of the external loading factor (the inverse of the external Q-factor) of the resonator for each coupling arrangement.

2.3.2 Hole coupling between cavities and microstrip

In order to combine the high inherent Q-factor and frequency stability of a cavity with the advantages of MIC-design, hole coupling between a TE_{01n} -cavity of circular cross-section and a microstrip line has been analyzed in the context of a previous contract. In the present report it is shown that the agreement between theoretical and experimental

results is improved considerably in the case of large coupling apertures if the external loading factor is evaluated on the basis of the average rather than the maximum magnetic field over the hole area. Fig. 4 shows a typical arrangement for microstrip-to-cavity coupling through a hole in the common grandplane.

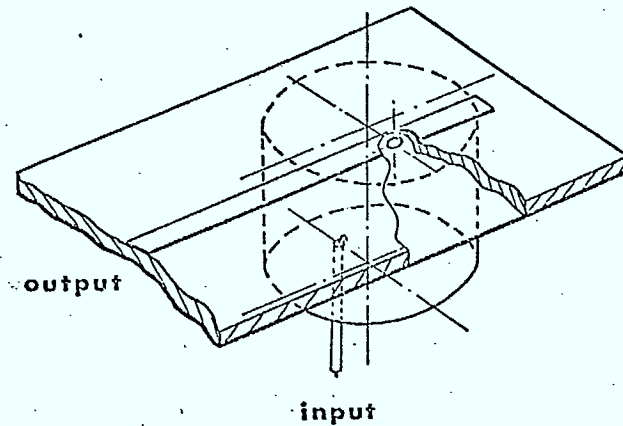


Fig. 4 Microstrip-to-Cavity coupling through a hole.

2.3.3 Hole coupling between rectangular waveguide and microstrip

The transition from a waveguide to microstrip through a single hole in a common wall has been evaluated. Fig. 5 depicts the fundamental arrangement the properties of which

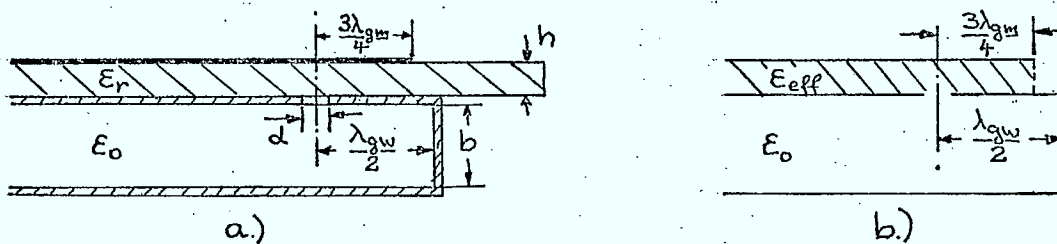


Fig. 5 Hole coupling between rectangular waveguide and microstrip a) actual structure, b) model representation.

may serve as a basis for the study of multi-hole transitions and directional couplers.

2.4 MICROSTRIP DISCONTINUITIES

The equivalent lumped element parameters of thin transverse metallic obstacles and transverse metallic posts of cylindrical cross-section have been calculated and measured. Fig. 6 shows such obstacles which possess geometries similar to coax-to-microstrip transitions or diode packages mounted across a microstrip line.

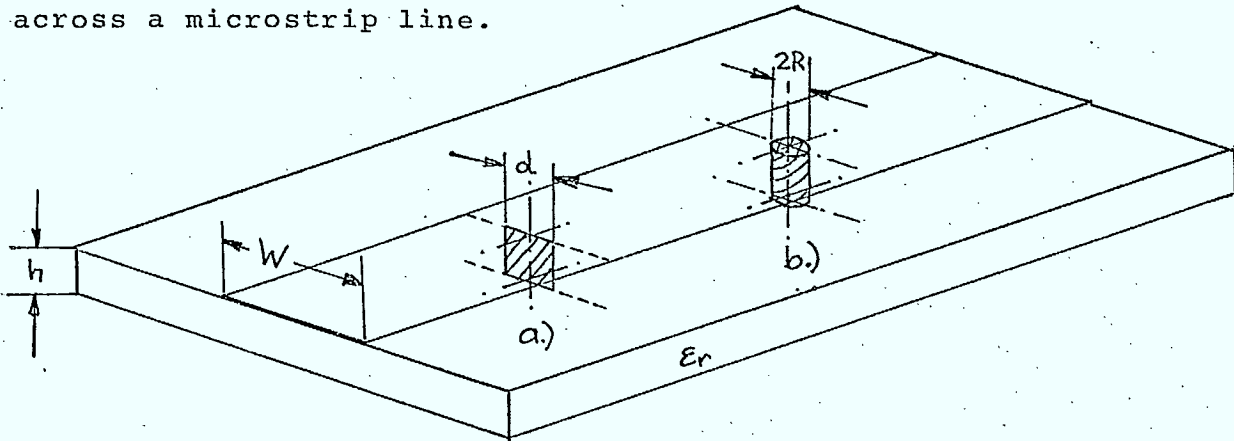


Fig. 6 Thin transverse obstacle (a) and cylindrical post (b) in a microstrip line.

Radiation from these obstacles has also been evaluated, and measurements of their Z-parameters have been made in a resonant microstrip ring.

In the following paragraph, the analytical approach to each of the aforementioned structures will be described, and theoretical expressions for their design parameters will be given.

3. ANALYSIS OF SELECTED STRUCTURES

3.1 MODES OF PROPAGATION IN THE MICROSTRIP MODEL

The parameters of the parallel plate model with magnetic sidewalls were first obtained by Wheeler¹ through conformal mapping of the static field between strips separated by a dielectric sheet. More accurate values for the characteristic impedance Z_0 may be obtained by calculating the capacitance per

unit length of the microstrip with a finite difference routine. Then ϵ_{eff} may be determined via Getsinger's² microstrip dispersion model. Finally, the dimensions of the model are given by the expression in Fig. 1.

The solutions of the homogeneous wave equation in this model - unpublished as yet - are similar to the modes in a rectangular waveguide, with the exception of the TEM-mode. They are in the coordinate system of Figure 1:

$$E_x = 0 \quad (1)$$

$$E_y = \pm V_o (Ah)^{-\frac{1}{2}} e^{\pm j\gamma z} \quad (2)$$

$$E_z = 0 \quad (3)$$

$$H_x = I_o (Ah)^{-\frac{1}{2}} e^{\pm j\gamma z} \quad (4)$$

$$H_y = 0 \quad (5)$$

$$H_z = 0 \quad (6)$$

Characteristic impedance:

$$Z_o = \zeta h/A = \zeta_o (\epsilon_{\text{eff}})^{-\frac{1}{2}} h/A \quad (7)$$

Cutoff wavelength:

$$\lambda_{co} = \infty \quad (8)$$

Propagation constant:

$$\gamma = \omega (\epsilon_o \epsilon_{\text{eff}} \mu_o)^{\frac{1}{2}} = (\omega/c) \epsilon_{\text{eff}}^{\frac{1}{2}} \quad (9)$$

TEM-Mode in an ideal parallel plate waveguide with magnetic sidewalls (Microstrip model, height h, width A)

$$E_x = \mp V_i' \cdot j \frac{(\epsilon_m \epsilon_n)^{\frac{1}{2}}}{A} m \cdot K \sin(m\pi x/A) \sin(n\pi y/h) e^{\pm j\gamma_i' z} \quad (10)$$

$$E_y = \pm V_i' \cdot j \frac{(\epsilon_m \epsilon_n)^{\frac{1}{2}}}{h} n \cdot K \cos(m\pi x/A) \cos(n\pi y/h) e^{\pm j\gamma_i' z} \quad (11)$$

$$E_z = I_i' \frac{(\epsilon_m \epsilon_n)^{\frac{1}{2}} \zeta \lambda}{2Ah} K^{-1} \cos(m\pi x/A) \sin(n\pi y/h) e^{\pm j\gamma_i' z} \quad (12)$$

$$H_x = I_i' \cdot j \frac{(\epsilon_m \epsilon_n)^{\frac{1}{2}}}{h} n \cdot K \cos(m\pi x/A) \cos(n\pi y/h) e^{\pm j\gamma_i' z} \quad (13)$$

$$H_y = I_i' \cdot j \frac{(\epsilon_m \epsilon_n)^{\frac{1}{2}}}{A} m \cdot K \sin(m\pi x/A) \sin(n\pi y/h) e^{\pm j\gamma_i' z} \quad (14)$$

$$H_z = 0 \quad (15)$$

$$\text{with } \epsilon_m = \begin{cases} 1 & \text{if } m = 0 \\ 2 & \text{if } m \neq 0 \end{cases} \quad \epsilon_n = \begin{cases} 1 & \text{if } n = 0 \\ 2 & \text{if } n \neq 0 \end{cases}$$

$$\text{and } K = (m^2 h/A + n^2 A/h)^{-\frac{1}{2}} \quad (16)$$

Characteristic Impedance:

$$Z_i' = V_i'/I_i' = \zeta \lambda / \lambda_{gi}' = \zeta [1 - (\lambda/\lambda_{ci}')^2]^{\frac{1}{2}} \quad (17)$$

Cutoff Wavelength:

$$\lambda_{ci}' = 2\pi/k_{ci}' = 2\pi [(m\pi/A)^2 + (n\pi/h)^2]^{-\frac{1}{2}} \quad (18)$$

Propagation Constant:

$$\gamma_i' = [\omega^2 \epsilon_o \epsilon_{eff} \mu_o - (m\pi/A)^2 - (n\pi/h)^2]^{\frac{1}{2}} \quad (19)$$

TM-Modes in an ideal parallel plate waveguide with magnetic sidewalls (Microstrip model, height h, width A)

$$E_x = V_i'' \cdot j \frac{(\epsilon_m \epsilon_n)^{\frac{1}{2}}}{h} n \cdot K \sin (m\pi x/A) \sin (n\pi y/h) e^{\pm j\gamma_i'' z} \quad (20)$$

$$E_y = V_i'' \cdot j \frac{(\epsilon_m \epsilon_n)^{\frac{1}{2}}}{A} m \cdot K \cos (m\pi x/A) \cos (n\pi y/h) e^{\pm j\gamma_i'' z} \quad (21)$$

$$E_z = 0 \quad (22)$$

$$H_x = \pm I_i'' \cdot j \frac{(\epsilon_m \epsilon_n)^{\frac{1}{2}}}{A} m \cdot K \cos (m\pi x/A) \cos (n\pi y/h) e^{\pm j\gamma_i'' z} \quad (23)$$

$$H_y = \mp I_i'' \cdot j \frac{(\epsilon_m \epsilon_n)^{\frac{1}{2}}}{h} n \cdot K \sin (m\pi x/A) \sin (n\pi y/h) e^{\pm j\gamma_i'' z} \quad (24)$$

$$H_z = V_i'' \frac{(\epsilon_m \epsilon_n)^{\frac{1}{2}} \lambda}{2\zeta A h} \cdot K^{-1} \sin (m\pi x/A) \cos (n\pi y/h) e^{\pm j\gamma_i'' z} \quad (25)$$

$$\text{with } \epsilon_m = \begin{cases} 1 & \text{if } m = 0 \\ 2 & \text{if } m \neq 0 \end{cases} \quad \epsilon_n = \begin{cases} 1 & \text{if } n = 0 \\ 2 & \text{if } n \neq 0 \end{cases}$$

$$\text{and } K = (m^2 h/A + n^2 A/h)^{-\frac{1}{2}} \quad (26)$$

Characteristic Impedance:

$$Z_i'' = V_i''/I_i'' = \zeta \lambda_{gi}'' / \lambda = \zeta [1 - (\lambda/\lambda_{ci}'')^2]^{-\frac{1}{2}} \quad (27)$$

Cutoff Wavelength:

$$\lambda_{ci}'' = 2\pi/k_{ci}'' = 2\pi [(m\pi/A)^2 + (n\pi/h)^2]^{-\frac{1}{2}} \quad (28)$$

Propagation Constant:

$$\gamma_i'' = [\omega^2 \epsilon_o \epsilon_{eff} \mu_o - (m\pi/A)^2 - (n\pi/h)^2]^{\frac{1}{2}} \quad (29)$$

TE-Modes in an ideal parallel plate waveguide with magnetic sidewalls (Microstrip model, height h, width A)

The field patterns of some of these modes have been sketched by Wolff et al.³ Even though the modes in the model describe the actual microstrip modes only to a first order approximation, they improve the solution of certain discontinuity problems over the results obtained with static approaches as will be seen in section 3.4 of the present report.

3.2 MODES OF RESONANCE IN TRIANGULAR PLANAR RESONATORS

The straightforward boundary conditions of the resonator model shown in Fig. 2b can be related to the conditions of a triangular waveguide by duality. A complete set of solutions for the latter problem has been described by Schelkunoff⁴ and was applied to the problem of resonances in triangular shaped ferrite posts by Akaiwa⁵.

Let a triangular resonator with magnetic sidewalls be filled with a dielectric material of scalar permittivity $\epsilon = \epsilon_0 \epsilon_r$ and permeability $\mu = \mu_0$. Among all the possible resonant modes, only the so-called $TM_{l,m,n;0}$ modes are of interest in microstrip applications. These modes exhibit an electric field which is independent of the z-coordinate (in the direction of thickness) and normal to the electric top and bottom walls of the resonator. The normalized expression for the electric field, as derived from Schelkunoff's⁴ formulae by Akaiwa⁵, is as follows:

$$\vec{E}(x,y,z,t) = \psi(x,y) e^{j\omega t} \vec{k} \quad (30)$$

$$\begin{aligned} \psi(x,y) = & \cos \left[\frac{2\pi}{3B} l \left(\frac{x}{2} + B \right) \right] \cos \frac{\sqrt{3}\pi(m-n)y}{9B} \\ & + \cos \left[\frac{2\pi}{3B} m \left(\frac{x}{2} + B \right) \right] \cos \frac{\sqrt{3}\pi(n-1)y}{9B} \\ & + \cos \left[\frac{2\pi}{3B} n \left(\frac{x}{2} + B \right) \right] \cos \frac{\sqrt{3}\pi(1-m)y}{9B} \end{aligned} \quad (31)$$

The magnetic field is obtained from (30) via Maxwell's equation:

$$\vec{H} = \frac{j}{\omega \mu} \text{curl } \vec{E} \quad (32)$$

The resonant frequencies are

$$f_{o_{1,m,n;0}} = \frac{1}{2} (\epsilon \mu)^{-\frac{1}{2}} \left[\left(\frac{4}{3A} \right)^2 (m^2 + mn + n^2) \right]^{\frac{1}{2}} \quad (33)$$

l, m and n are integers which never take zero value simultaneously and satisfy the following condition

$$l + m + n = 0 \quad (34)$$

The lowest resonant frequency occurs for the following combinations:

$$\begin{array}{lll} l = 0 ; & m = 1 ; & n = -1 \\ l = -1 ; & m = 0 ; & n = 1 \\ l = -1 ; & m = 1 ; & n = 0 \end{array}$$

The corresponding field configuration could be described as a quasi-TEM wave propagating in a tapered microstrip which is open-circuited at the wide end. The field distribution function $\psi(x, y)$ is for the fundamental mode :

$$\begin{aligned} \psi(x, y) = & 2 \cos \frac{2\pi}{3B} \left(\frac{x}{2} + B \right) \cos \frac{\sqrt{3}\pi}{9B} y \\ & + \cos \frac{2\sqrt{3}\pi}{9B} y \end{aligned} \quad (35)$$

This expression may be normalized by writing

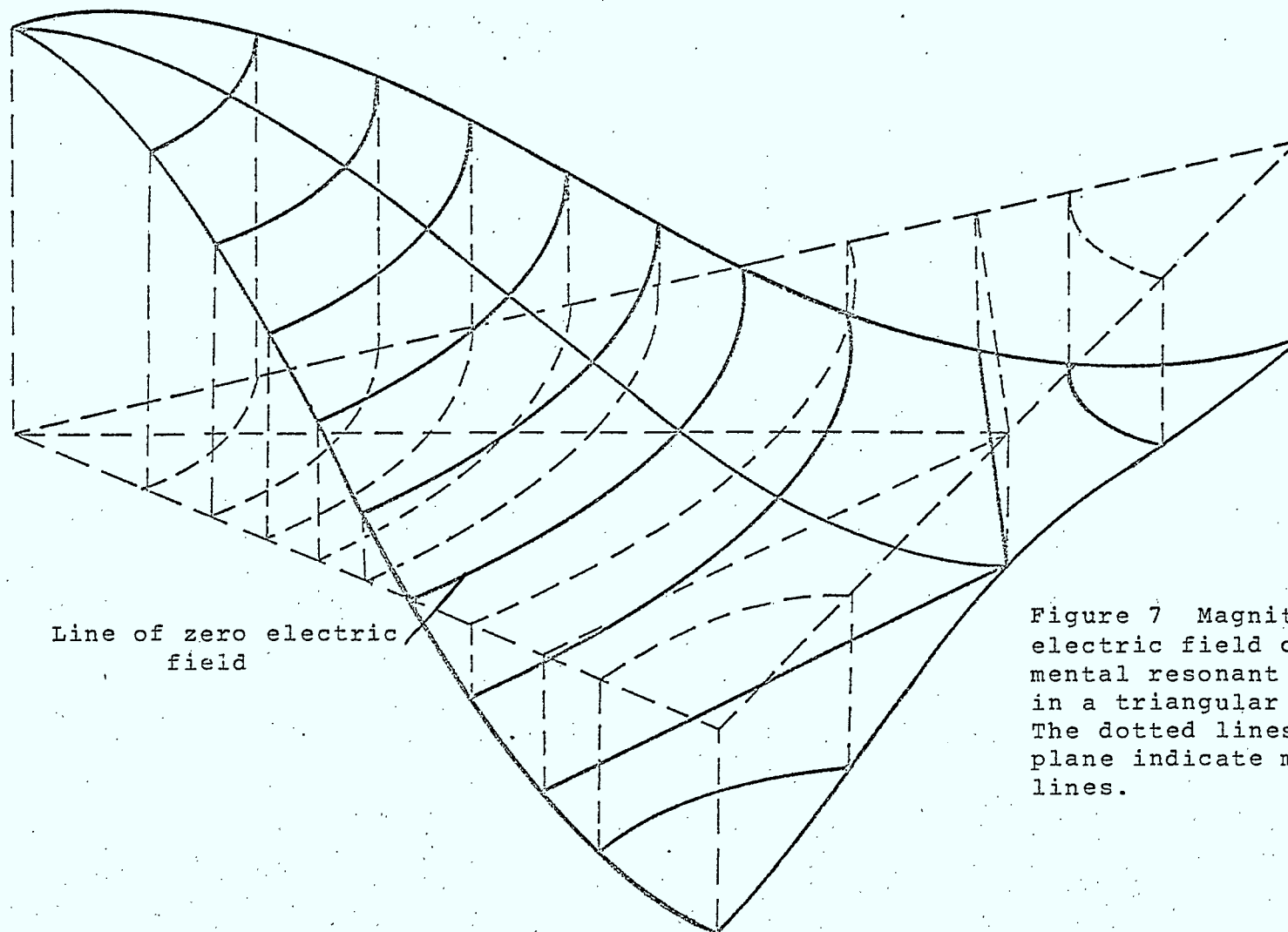
$$\frac{x}{B} = X \quad ; \quad \frac{y}{B} = Y \quad (36)$$

Thus

$$\begin{aligned} \psi(X, Y) = & 2 \cos \frac{2\pi}{3} \left(\frac{X}{2} + 1 \right) \cos \frac{\sqrt{3}\pi}{9} Y \\ & + \cos \frac{2\sqrt{3}\pi}{9} Y \end{aligned} \quad (37)$$

This function is represented graphically in Fig. 7.

Lines of constant value for $\psi(X, Y)$ are drawn and projected upon the X-Y plane, representing the magnetic field lines of the fundamental mode in the triangular resonator.



Line of zero electric
field

Figure 7 Magnitude of the
electric field of the funda-
mental resonant mode ($TM_{0,1,-1;0}$)
in a triangular resonator.
The dotted lines in the triangular
plane indicate magnetic field
lines.

For the analysis of coupling arrangements and the evaluation of Q-factors associated with the modes, the energy stored in the resonator is of particular interest. The stored energy is obtained as the volume integral taken over the square of the mode function $\psi(x,y)$ in the resonator as follows:

$$W_{\text{stored}} = \frac{1}{2} \epsilon \int_{V_{\text{res}}} [\psi(x,y)]^2 dv \quad (38)$$

For a triangular resonator of height h and side $A = 2\sqrt{3}B$, this integral becomes

$$W_{\text{stored}} = \epsilon h B^2 \cdot I = \frac{1}{12} \epsilon h A^2 \cdot I \quad (39)$$

where I is given by the following expression:

$$\begin{aligned} I = \frac{3\sqrt{3}}{8} \bigg\{ & 3 + 2 [SI(2\pi l) + SI(2\pi m) + SI(2\pi n)] \\ & + (1 + 2\frac{l^2}{mn}) SI^2(\pi l) + (1 + 2\frac{m^2}{ln}) SI^2(\pi m) + (1 + 2\frac{n^2}{lm}) SI^2(\pi n) \\ & + [2(\frac{m-n}{m-1} + \frac{m-n}{1-n}) - 1] SI^2[\frac{\pi}{3}(m-n)] \\ & + [2(\frac{n-1}{m-1} + \frac{n-1}{n-m}) - 1] SI^2[\frac{\pi}{3}(n-1)] \\ & + [2(\frac{1-m}{1-n} + \frac{1-m}{n-m}) - 1] SI^2[\frac{\pi}{3}(1-m)] \\ & + [4 + \frac{m-1}{m-n} + \frac{m-1}{n-1}] SI^2[\frac{2\pi}{3}(m-1)] \\ & + [4 + \frac{1-n}{m-n} + \frac{1-n}{1-m}] SI^2[\frac{2\pi}{3}(1-n)] \\ & + [4 + \frac{n-m}{n-1} + \frac{n-m}{1-m}] SI^2[\frac{2\pi}{3}(n-m)] \bigg\} \quad (40) \end{aligned}$$

In this expression, $SI^2(x) = (\frac{\sin x}{x})^2$. l , m and n are the integers described earlier (see equ. 3).

Note that

$$SI(x) = \begin{cases} 1 & \text{for } x = 0 \\ 0 & \text{for } x = \pm i\pi, i = 1, 2, 3, 4, \dots \end{cases}$$

Also

$$\frac{2\ell^2}{mn} \sin^2(\pi\ell) = 0 \quad (41)$$

whenever one of the three indices (l; m; n) is zero. The integral I (equ. 40) can take two distinct values as follows:

If one of the three indices l, m or n is zero or if two of the indices l, m and n are identical (i.e. l = k, m = k, n = -2k, then $I = 9\sqrt{3}/4$.

But if all three indices differ from each another - excluding the value zero for one of them - , then $I = 9\sqrt{3}/8$. This fact is presented in a compact fashion in Table 1.

l = 0	m = k	n = -k	}	$I = 9\sqrt{3}/4$
l = k	m = 0	n = -k		
l = k	m = -k	n = 0		
l = k	m = k	n = -2k		
l = k	m = -2k	n = k		
l = -2k	m = k	n = k		
l ≠ m ≠ n	and simultaneously		}	$I = 9\sqrt{3}/8$
l ≠ 0				
m ≠ 0		n ≠ 0		

Table I Values for the Integral I (equ. 40) as a function of the values of the mode indices l, m and n.

The following section on coupling arrangements will repeatedly refer to the expressions for fields and stored energy derived above.

3.3 COUPLING BETWEEN MICROSTRIP AND SELECTED STRUCTURES

3.3.1 Hole coupling between microstrip and a cavity

Small coupling apertures act as radiating dipoles when excited by a microwave field. On the basis of this concept, Wheeler⁶ has derived simple expressions to evaluate aperture coupling between resonant cavities or waveguides in terms of volume ratios. Hoefer and James⁷ have extended the method to the coupling between microstrip and cavities. A theoretical expression for the loading power factor $p = 1/Q_{\text{ext}}$ of a cavity (resonating in the cylindrical TE_{01n} - mode) has been derived and was found to be in good agreement with experimental values for coupling holes small compared with the guided wavelength in the microstrip. However, coupling through larger holes turned out to be weaker than predicted, due to the nonuniform distribution of the magnetic field over the hole area; initially, analysis was based on the assumption that this field was constant over the aperture.

Agreement between theory and measurement can be considerably improved by employing the average magnetic field over the hole instead of its maximum value in the calculation of the hole reactance. When the wavelength in the microstrip becomes so short (large dielectric constant of the substrate, high frequency) that the hole dimensions are no longer small compared with the wavelength, a first order correction amounts to multiplying the expression for the loading power factor p by $(H_{\text{average}}/H_{\text{max}})^2$.

The average value H_{average} is obtained by integrating the expression for the magnetic field over the hole area and dividing the integral by the aperture surface. Figure 8 shows the situation in which all dimensions have been normalized to the hole radius.

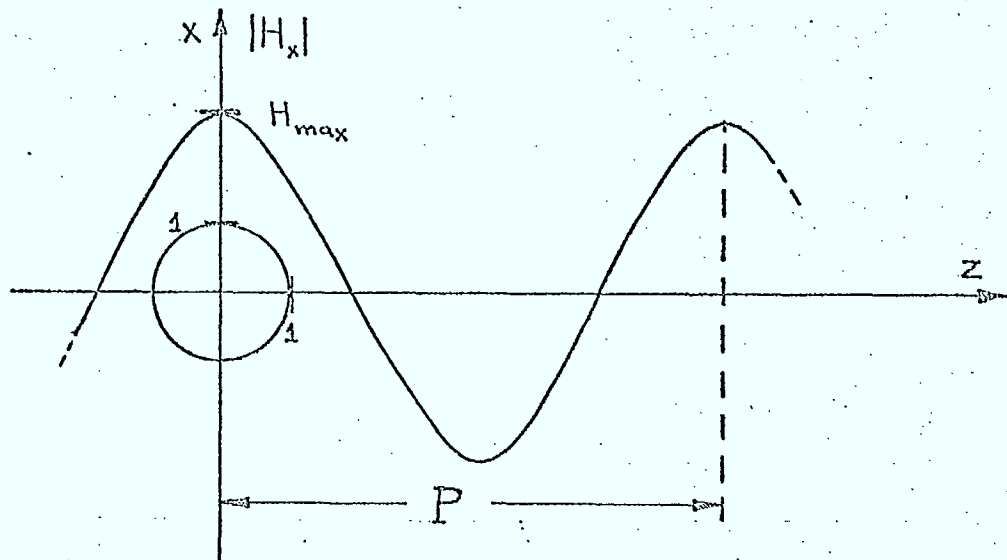


Figure 8 Field distribution over the circular aperture in the microstrip.

The magnetic field is given by the expression:

$$\vec{H} = H_{\max} \cos \frac{2\pi}{P} \cdot z \cdot \vec{u}_z \quad (42)$$

where P is the normalized guided wavelength on the microstrip ($P = .2\lambda_g / d$), λ_g = wavelength and d = hole diameter. The average value of the magnetic field over the hole area is given by the following expression:

$$H_{\text{average}} = \frac{\int \int_{\text{Hole area}} H_{\max} \cos \left(\frac{2\pi}{P} z \right) dx dz}{\text{Hole area}} = \frac{\int_0^1 \int_0^{\sqrt{1-z^2}} H_{\max} \cos \left(\frac{2\pi}{P} z \right) dx dz}{\pi/4} \quad (43)$$

Integration with respect to x yields

$$H_{\text{average}} = \frac{4}{\pi} H_{\max} \int_0^1 \sqrt{1-z^2} \cos kz dz \quad (44)$$

where $2\pi/P$ has been replaced by the symbol k .

The bounded integral in eqn. (3) is a constituent of an integral representation of the Bessel-Funktion $J_1(k)$ (see ²)

$$J_1(k) = \frac{k}{\Gamma(\frac{1}{2}) \Gamma(\frac{3}{2})} \int_0^1 \sqrt{1-z^2} \cos kz \, dz \quad (45)$$

Thus, the integral itself becomes

$$\int_0^1 \sqrt{1-z^2} \cos kz \, dz = \frac{J_1(k) \Gamma(\frac{1}{2}) \Gamma(\frac{3}{2})}{k} = \frac{\pi}{2k} J_1(k) \quad (46)$$

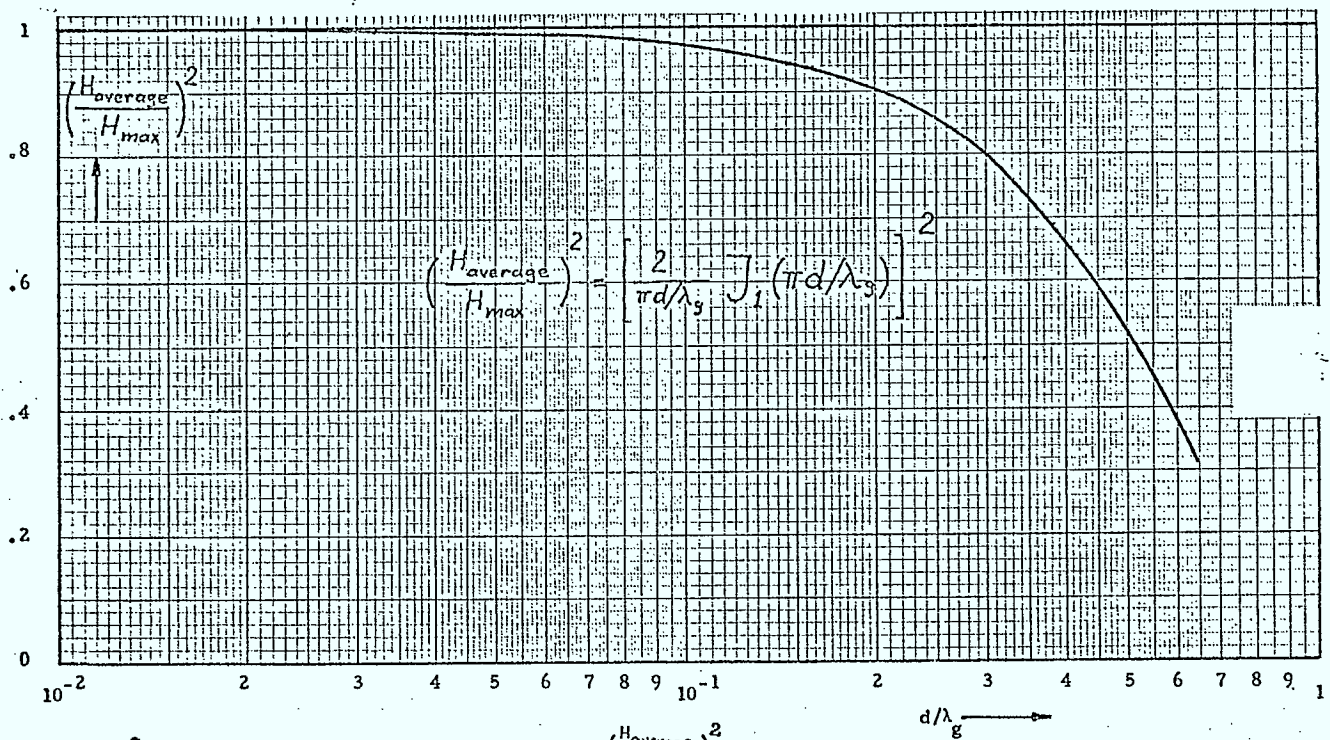


Figure 9 Graphical representation of the function $\left(\frac{H_{\text{average}}}{H_{\text{max}}}\right)^2$

The average magnetic field is then

$$H_{\text{average}} = H_{\text{max}} \frac{2}{k} J_1(k) = H_{\text{max}} \frac{2}{\pi d / \lambda_g} J_1(\pi d / \lambda_g) \quad (47)$$

Application of the correction factor $(H_{\text{average}}/H_{\text{max}})^2$, which is represented in figure 9, to the expression for the loading power factor⁷ yields

$$p = 0.09399 \frac{d^4 n^2 \lambda_o^2 \lambda_g}{L^3 D^2 A h} [J_1(\pi d / \lambda_g)]^2 \quad (48)$$

This expression is represented as a dashed curve in figures 10 and 11. It can be seen that for large aperture diameters, the corrected curve fits the experimental values better than the uncorrected one, while for small apertures, the uncorrected curve predicts the measured values very well.

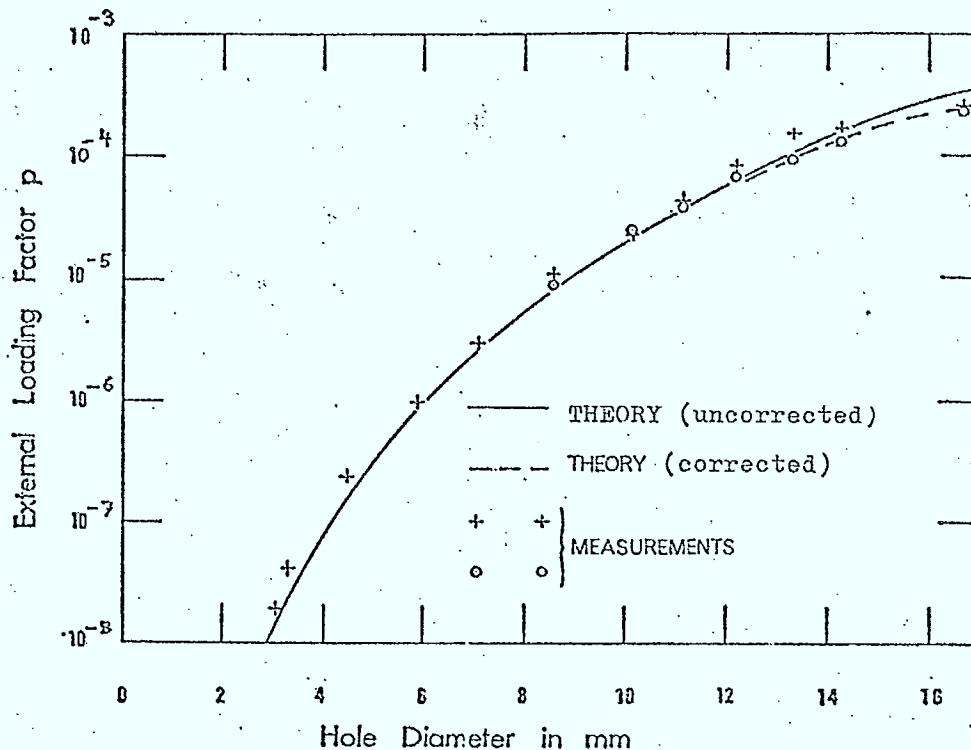


Figure 10 Uncorrected and corrected theoretical curves for p are compared with experimental values (TE_{012} cavity coupled to 50 Ohm microstrip on Rexolite, $\epsilon_r = 2.6$)

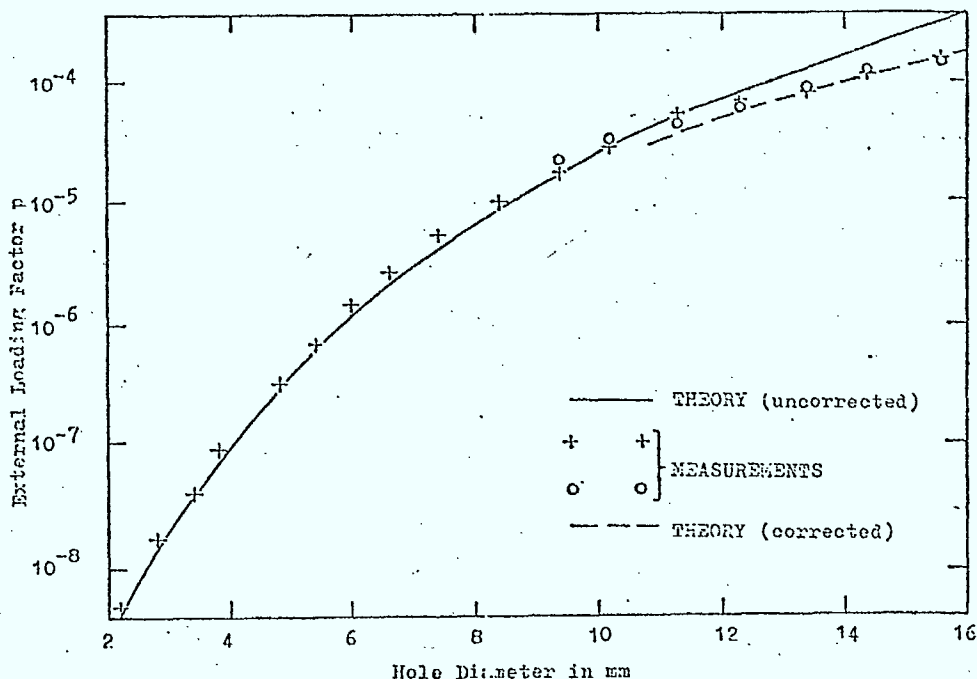


Figure 11 Uncorrected and corrected theoretical curves for p are compared with experimental values (TE_{012} cavity coupled to 23 Ohm microstrip on Stycast, $\epsilon_r = 10.8$)

3.3.2 Hole coupling between microstrip and a triangular planar resonator

The analysis of this coupling problem (see Fig. 12) goes along the same lines as the preceding section on microstrip to cavity coupling. The only difference resides in the expression for energy stored in the resonator which results in a different value for Wheeler's⁶ effective resonator volume in the formula for the external loading factor p :

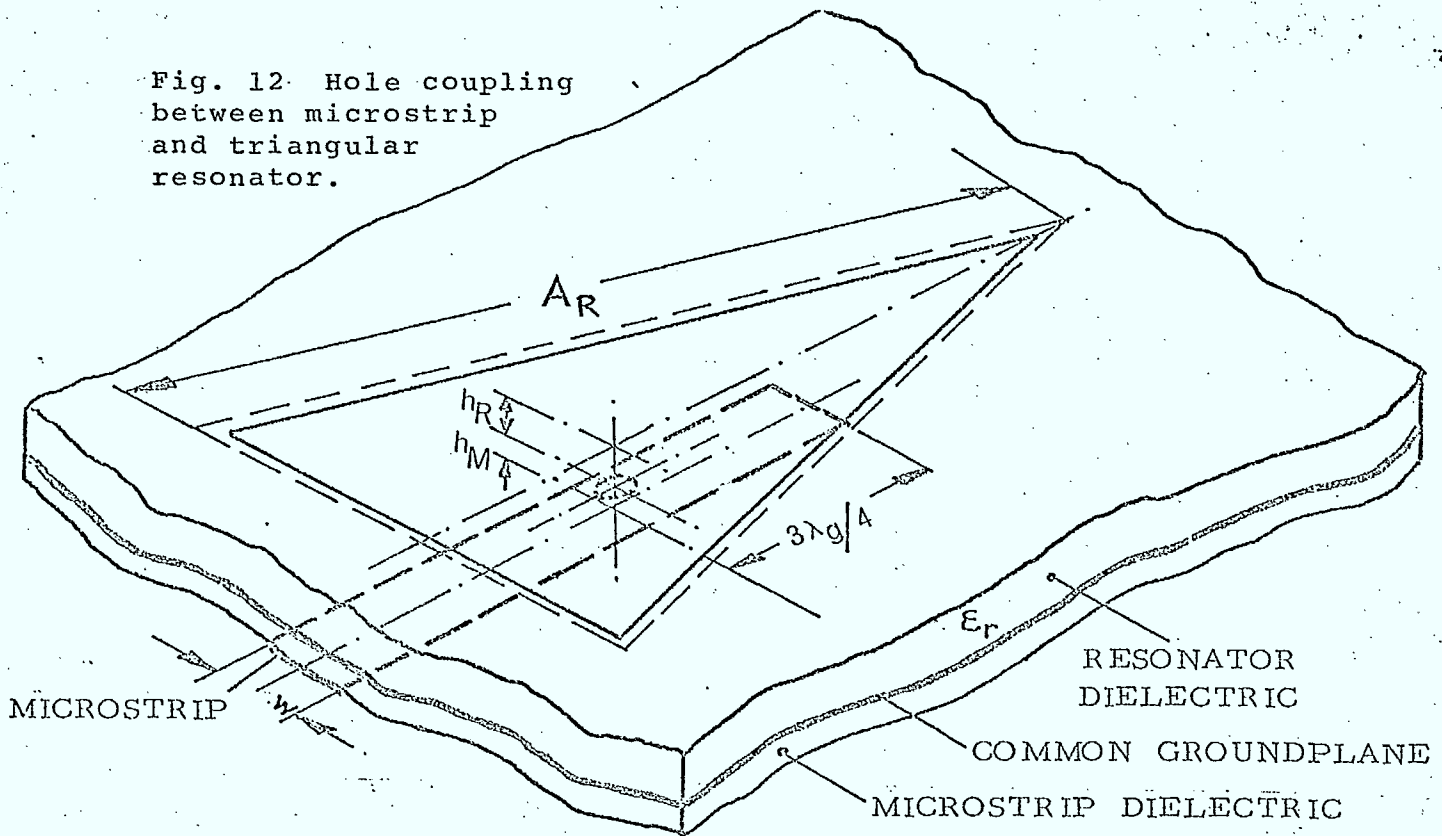
$$p = x \cdot k$$

(49)

Where x is the normalized coupling reactance between two identical microstrip lines connected by the coupling aperture, and k is the factor of coupling between two identical triangular

resonators connected by the same aperture. While x is the same as in the microstrip to cavity coupling problem (see reference 7), the factor k becomes

Fig. 12 Hole coupling between microstrip and triangular resonator.



$$k \quad \frac{1}{4} = \frac{V_{mc}}{V_m} \quad (50)$$

where V_{mc} is the effective volume of the coupling aperture ($V_{mc} = 2d^3/3$ for a circular hole of diameter d) and V_m is the effective volume of the resonator defined by the following equation

$$V_m = (\frac{1}{2}\mu \int_{V_{res}} |\vec{H}|^2 dv) / (\frac{1}{2}\mu |\vec{H}_c|^2) \quad (51)$$

In this expression, H_c is the tangential magnetic field in the resonator at the position of the hole.

The numerator of eqn. (51) is the energy stored in the resonator and therefore equal to the equivalent volume integral over the electric field:

$$\frac{1}{2} \mu_0 \int_{V_{res}} |\vec{H}|^2 dv = \frac{1}{2} \epsilon_0 \epsilon_r \int_{V_{res}} |\vec{E}|^2 dv = \frac{1}{2} \epsilon_0 \epsilon_r \int_{V_{res}} [\psi(x,y)]^2 dv \quad (52)$$

On the other hand, the magnetic field at the aperture can be expressed as a function of the electric field and is in view of eqn. (32):

$$\vec{H}_c(x_c, y_c) = \frac{j}{\omega_0 \mu_0} |\text{curl} [\psi(x,y)] \cdot \vec{k}|_{x_c, y_c} \quad (53)$$

where x_c, y_c are the coordinates of the coupling hole. Equation (52) has already been evaluated [see (39), (40) and Table 1 for the value of the integral]. We thus obtain the following expression for the effective volume of the triangular resonator:

$$V_m = \frac{1}{6} (\omega_0/c)^2 \epsilon_r h_R A_R^2 I |\text{curl} [\psi(x,y)] \vec{k}|_{x_c, y_c}^{-2} \quad (54)$$

The external loading factor is then in view of equations (49), (50), and (54):

$$p = \frac{1}{3} (\pi d^6 c^2) |\text{curl} \psi(x,y) \vec{k}|_{x_c, y_c}^2 / (I A_M h_M h_R A_R^2 \lambda_g^2 \omega_0^2 \epsilon_r) \quad (55)$$

where

- d = Diameter of the coupling hole
- c = speed of light
- A_M = Width of microstrip model
- h_M = Height of microstrip model
- A_R = Side length of resonator model
- h_R = Height of resonator model
- λ_g = Guided wavelength (TEM) in microstrip at resonance
- ω_0 = Resonant angular frequency
- ϵ_r = Rel. dielectric constant of resonator dielectric
- I = Integral as given in eqn. (40)
- ψ = Field distribution function in the resonator as defined in eqn. (35).

The particular case of coupling to the fundamental mode through a circular hole in the centre of the triangular resonator is presented in Fig. 12. If the hole diameter d is a relatively large fraction of the wavelength λ_g in the microstrip, p must be corrected by multiplying eqn. (55) by the factor $(H_{average}/H_{max})^2$ represented in Fig. 9.

3.3.3 Hole coupling between waveguide and a triangular planar resonator

This problem differs from the preceding case only by the expression for the hole reactance x .

$$x = \frac{2\pi d^3}{3ab\lambda_g} \quad (\text{circular iris}) \quad (56)$$

In view of equations (49), (50), (54) and (56), the external loading factor p becomes:

$$p = \frac{2}{3} (\pi d^6 c^2) \left| \text{curl } \psi(x, y) \vec{k} \right|_{x_c, y_c}^2 / (I a b h_R A_R^2 \lambda_g^2 \omega_o^2 \epsilon_r) \quad (57)$$

where

- d = Diameter of the coupling hole
- c = Speed of light
- a = Width of waveguide cross-section
- b = Height of waveguide cross-section
- A_R = Side length of resonator model
- h_R = Height of resonator model
- λ_g = Guided wavelength in the waveguide (TE_{10})
- ω_o = Angular resonant frequency
- ϵ_r = Relative dielectric constant of resonator dielectric
- I = Integral as given in eqn. (40)
- ψ = Field distribution function in the resonator as defined in eqn. (35).

Again, multiplication of p by a correction factor $(H_{\text{average}}/H_{\text{max}})^2$ [(see eqn. 76)] is in order for large fractions d/λ_g . Fig. 13 shows an example of the coupling situation described by eqn. (57). The same formula may be applied to an arrangement where the coupling hole is situated in the centre of the large wall of the waveguide at $n \cdot \lambda_g/2$ before a short circuit, as shown in Fig. 3c.

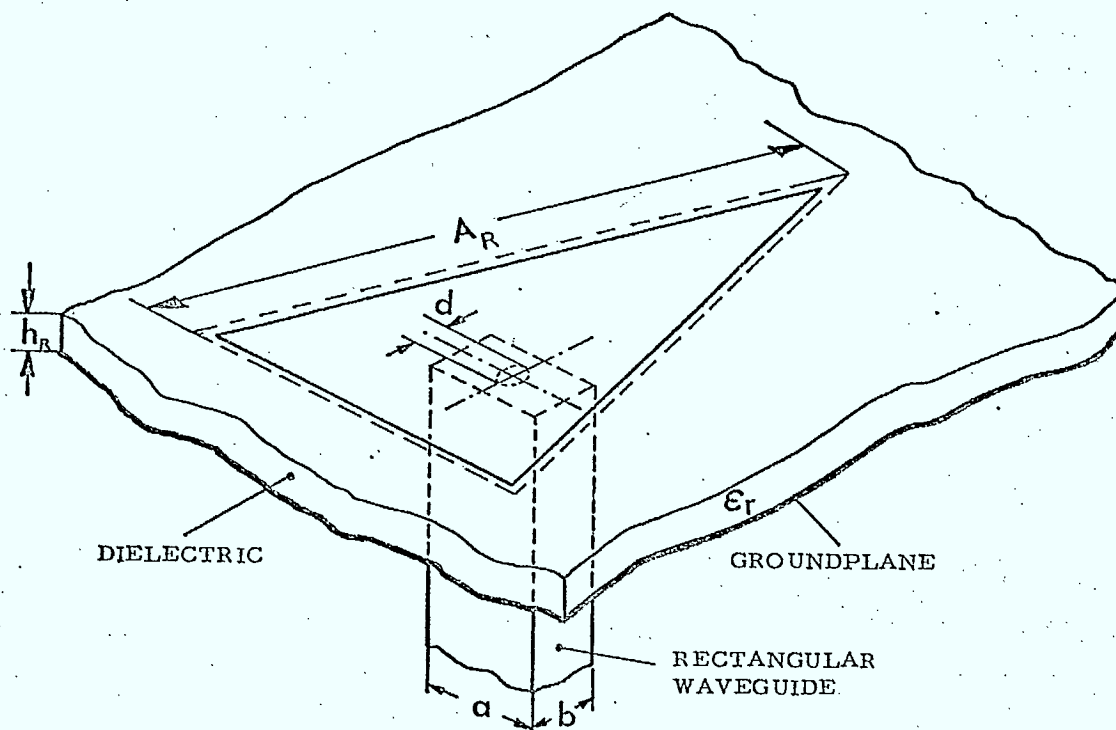


Figure 13 Hole coupling (magnetic) between waveguide and triangular planar resonator.

3.3.4 Galvanic (direct) coupling between microstrip and a triangular planar resonator

Two examples of galvanic coupling are shown in Fig. 3a. To evaluate the external loading factor of the resonator in these cases, let the centreline of the microstrip intersect the periphery of the resonator at (x_c, y_c) . If we assume that the microstrip does not perturbate the field pattern in the resonator, the voltage across the microstrip line at (x_c, y_c) is V_c :

$$V_c = E_z(x_c, y_c) \cdot h_R = \psi(x_c, y_c) e^{j\omega_o t} \cdot h_R \quad (58)$$

If the microstrip is matched at the far end, the resonator is loaded at (x_c, y_c) with the characteristic impedance Z_o of the microstrip. The energy dissipated per cycle in the external load is then

$$W_d = V_{cmax}^2 / (2Z_o f_o) = [\psi(x_c, y_c)]^2 h_R^2 / (2Z_o f_o) \quad (59)$$

and the external loading factor p becomes

$$p = 1/Q_{ext} = \frac{\text{Energy dissipated in external load}}{2\pi \cdot \text{Energy stored in the resonator}} \\ = W_d / (2\pi \cdot W_{stored}) \quad (60)$$

where W_{stored} is given by eqn. (39) and W_d by eqn. (59). Thus

$$p = 3h_R [\psi(x_c, y_c)]^2 / (\pi f_o Z_o \epsilon_o \epsilon_r A_R^2 I) \quad (61)$$

I is again the integral defined in (40). ϵ_r is the dielectric constant of the resonator substrate of thickness h_R , f_o is the resonant frequency and A_R the side length of the triangular resonator model.

3.3.5 Capacitive coupling between microstrip and a triangular resonator

Arrangements of this kind are shown in Fig. 3b. The analysis of such a case is very similar to the evaluation of direct coupling, the difference being the additional coupling capacitor separating the impedance Z_o from the resonator. For the calculation of the external Q , the series combination of Z_o and C_s is conveniently transformed into a parallel combination of f_o . The resistive part of this parallel combination reflects the external losses while the capacitive part slightly affects the stored energy and thus the resonant frequency of the resonator. Figure 14 shows the equivalent circuit of such a capacitive coupling arrangement.

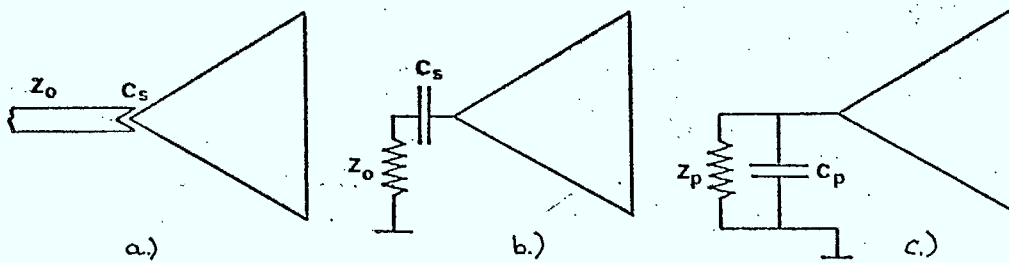


Figure 14 Capacitive coupling between microstrip and triangular resonator (a) and equivalent series (b) and parallel (c) circuits.

The value of the series coupling capacity C_s may be obtained with a numerical method or an empirical formula for such configurations. The equivalent parallel elements are then found as follows:

$$Z_p = \frac{1 + (\omega_0 C_s Z_0)^2}{Z_0 (\omega_0 C_s)^2} \quad (62)$$

$$C_p = \frac{C_s}{1 + (\omega_0 C_s Z_0)^2} \quad (63)$$

For the evaluation of the external loading factor, the effect of C_p can always be neglected. The expression for p , is then the same as (61) with Z_0 replaced by Z_p as given by (62):

$$p = 3h_R [\psi(x_c, y_c)]^2 / (\pi f_0 Z_p \epsilon_0 \epsilon_r A_R^2 I) \quad (64)$$

where all symbols are defined as in (61).

3.3.6 Hole coupling between waveguide and microstrip

A narrowband transition from microstrip to waveguide and vice-versa may be built using magnetic coupling through a common aperture. Analysis for small coupling holes may be done using Bethe's⁹ small hole theory. According to this

theory, a hole is equivalent to a radiating dipole the strength of which depends only on the incident field. The power radiated from the hole is independent of the configuration and characteristic impedance of the guide into which it radiates.

The power transmitted through the transition can thus be predicted by assuming that the hole connects two identical waveguides of the type from which the power is incident. Thus

$$\frac{P_{\text{transmitted}}}{P_{\text{incident}}} = \left(\frac{V_{\text{transmitted}}}{V_{\text{incident}}} \right)^2 \cdot \frac{Z_{01}}{Z_{02}} = \left(\frac{V_{\text{transmitted}}}{V_{\text{incident}}} \right)^2 \quad (65)$$

$Z_{01} = Z_{02}$

where Z_{01} is the characteristic impedance of the guide from which the power is incident and Z_{02} is the characteristic impedance of the guide into which power is transmitted.

Figure 15 shows an arrangement for hole coupling between waveguide and microstrip and its equivalent circuit. The normalized reactance of the coupling hole is different when measured from the waveguide and the microstrip side. In the case of a circular hole, these reactances are, as measured in the waveguide:

$$x_w = (2\pi d^3) / (3ab\lambda_{gw}) \quad (66)$$

as measured in the microstrip:

$$x_m = (\pi d^3) / (3Ah\lambda_{gm}) \quad (67)$$

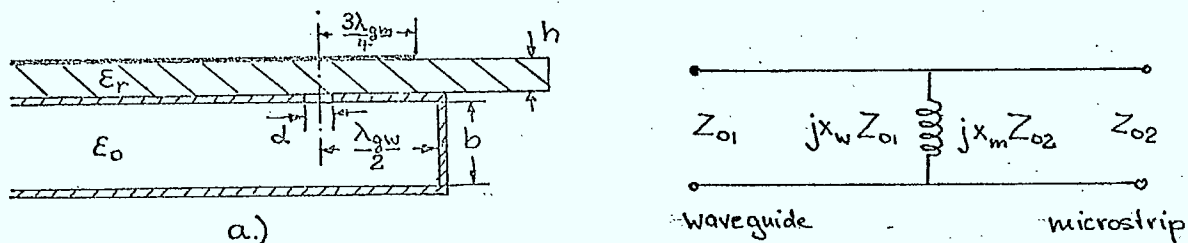


Fig. 15 Arrangement for hole coupling between microstrip and waveguide.

where d is the hole diameter, a and b are the sides of the waveguide, A and h the sides of the microstrip model (see Fig. 1), and λ_{gw} and λ_{gm} are the guided wavelengths in the waveguide and the microstrip respectively.

According to Montgomery¹⁰, the voltage transmission coefficient between two identical guides is

$$V_{tr}/V_{inc} = -\frac{2j}{B} \quad (68)$$

where $B = \frac{1}{x} =$ normalized susceptance of the hole. Thus

$$P_{tr}/P_{inc} = \frac{4}{B^2} = 4x^2 \quad (69)$$

Since this power transmission coefficient is independent of the characteristic impedances of the output guide, it becomes

For transmission from waveguide to microstrip:

$$P_{tr}/P_{inc} = 4 x \frac{2}{w} = [(4\pi d^3) / (3ab\lambda_{gw})]^2 \quad (70)$$

and for transmission from microstrip to waveguide:

$$P_{tr}/P_{inc} = 4 x \frac{2}{w} = [(2\pi d^3) / (3Ah\lambda_{gm})]^2 \quad (71)$$

In order to calculate the voltage transmission coefficients, characteristic impedances may be defined as follows:

For the waveguide,

$$Z_{ow} = \zeta_o \frac{\lambda_{gw}}{\lambda_o} \quad (\text{TE - modes}) \quad (72)$$

For the microstrip,

$$Z_{om} = \zeta_o \frac{h}{A} \sqrt{\frac{1}{\epsilon_{eff}}} \quad (\text{TEM - mode}) \quad (73)$$

In view of eqns. (65), (70), (71), (72), and (73), the voltage coefficient becomes

for transmission from waveguide to microstrip:

$$V_{tr}/V_{inc} = \frac{4\pi d^3}{3ab\lambda_{gw}} \left[(h\lambda_{gm}) / (A\lambda_{gw}) \right]^{\frac{1}{2}} \quad (74)$$

and for transmission from microstrip to waveguide:

$$V_{tr}/V_{inc} = \frac{2\pi d^3}{3Ah\lambda_{gm}} \left[(A\lambda_{gw}) / (h\lambda_{gm}) \right]^{\frac{1}{2}} \quad (75)$$

It must be kept in mind that these expressions are valid only for small apertures. A first order correction consists of multiplying the value of x in eqns. (66) and (67) by a factor $(H_{average}/H_{max})^2$ where $H_{average}$ is the average magnetic field taken over the hole area and H_{max} is the maximum magnetic field in the centre of the hole. The power transmission coefficient must thus be multiplied by a factor $(H_{average}/H_{max})^4$ to take into account the nonuniform field distribution over the hole area.

The correction factor for circular apertures in waveguides may be found in the same way as the corresponding factor for microstrip derived and presented in section 3.3.1. The only difference resides in the additional nonuniformity of the field in transverse direction in the case of the waveguide. Since this variation is also sinusoidal with a period of $2a$ (a = width of the waveguide), the correction factor is

$$(H_{average}/H_{max})^2 = \left[\frac{2\lambda_{gw}}{\pi d} J_1(\pi d/\lambda_{gw}) \right]^2 \left[\frac{4a}{\pi d} J_1(\pi d/2a) \right]^2 \quad (76)$$

Both terms may be obtained directly from Fig. 9 by reading d/λ_{gw} on the abscissa for the first term and $d/2a$ for the second term.

The logarithm of the power transmission coefficient for transmission from waveguide to microstrip has been calculated and presented in Figure 16. The effect of the first order correction is quite remarkable for values of $d/a > 0.3$.

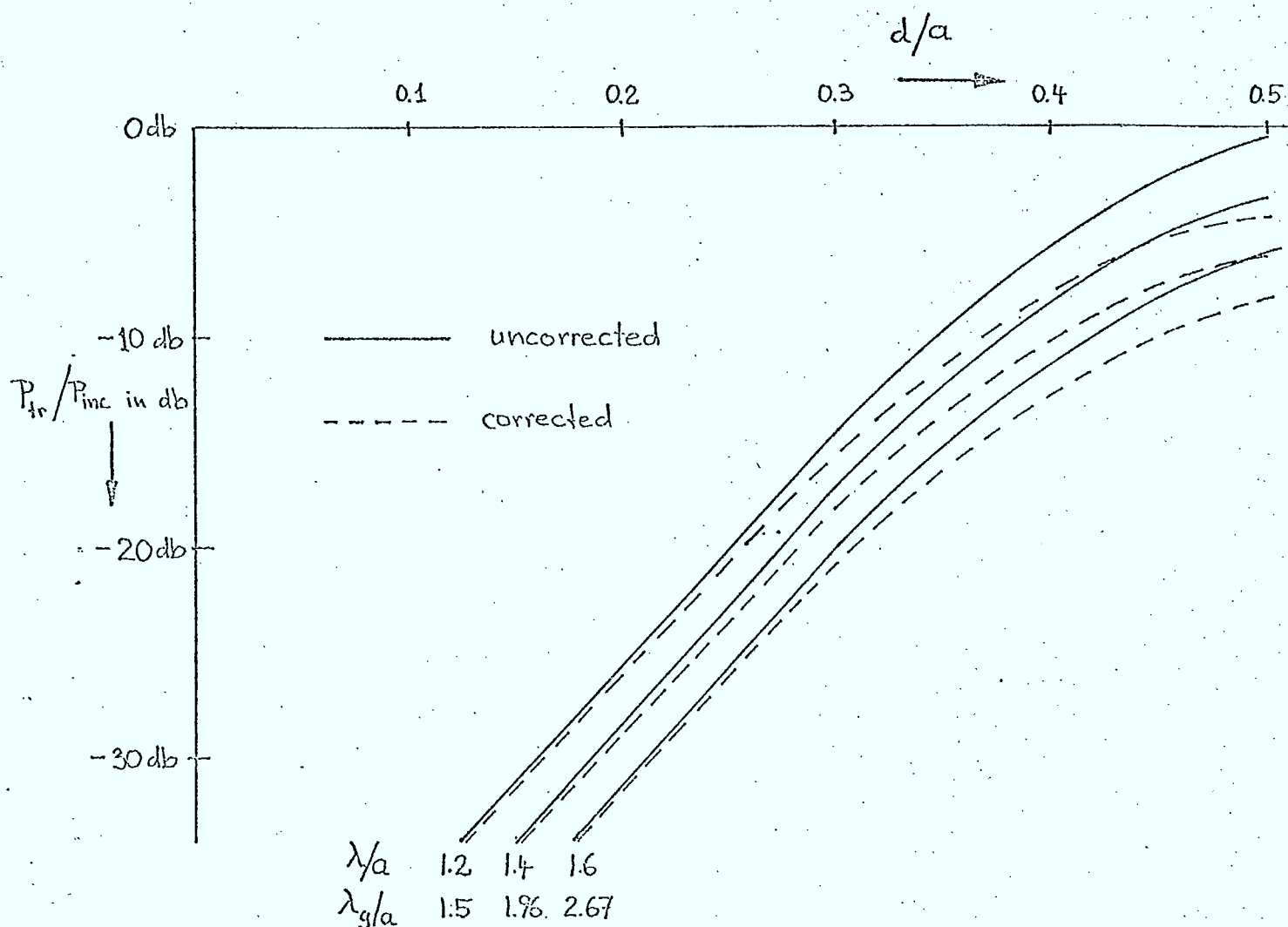


Fig. 16 Transmission through a circular hole from a waveguide ($a/b = 2.12$) to microstrip as a function of the hole diameter d and wavelengths λ (free space) and λ_{gw} . (Magnetic coupling as shown in Fig. 15).

The action of several holes could be combined to achieve directional coupling between microstrip and waveguides.

3.4 EQUIVALENT CIRCUIT OF TRANSVERSE MICROSTRIP DISCONTINUITIES

Lossless discontinuities in transmission lines can be represented by a T or π - section of three lumped reactances as shown by Schwinger and Saxon¹¹. If the discontinuity is symmetrical about a transverse plane ($z = 0$ plane, see Fig. 17,

the equivalent circuit is also symmetrical, and the fields on the line are conveniently represented as the sum of even and odd functions about this plane. The separation into even and odd cases leads to two variational expressions for the discontinuity reactance corresponding to the even and odd excitation respectively.

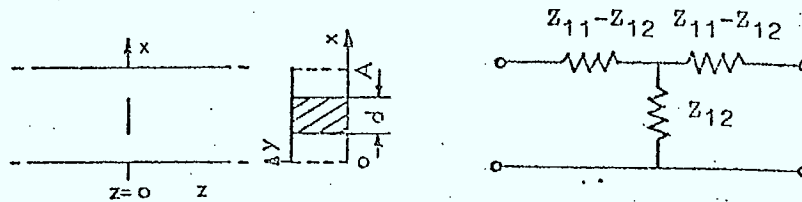


Fig. 17 Thin transverse obstacle in the microstrip model

Equivalent lumped element circuit in the $z = 0$ plane

The variational expressions for the discontinuity reactance contain a dynamic Green's function which must be derived for the particular type of transmission line. Since there is no such function available for microstrip to date, even for the dispersionless case, an approximate Green's function has been derived using Wheeler's¹ parallel plate model with magnetic sidewalls. (see figure 1). Even though this model describes fairly accurately the quasi-TEM mode propagation in a microstrip line, the higher modes in the model represent the field at the discontinuity to a first order approximation only. However, in the absence of an exact expression for higher modes in microstrip, the solution of the inhomogeneous wave equation in the model is preferable to a static approach. It can be expected that the analysis yields best results if the discontinuity is small with respect to the strip width and located close to the centre of the microstrip cross-section where the incident TEM-field is nearly homogeneous. It is always assumed that only the TEM-wave can propagate in the model whereas all higher modes are cut off.

The variational expressions for the discontinuity reactance.

Since the transverse electric field as well as the dimensions of the discontinuities considered in this study are independent of the y-coordinate, (see Fig.17), the problem is described by the following two-dimensional scalar wave equation:

$$\phi(x,z) = \phi^{inc}(x,z) + \int_{\text{obstacle}} G(x,z;x',z')K(x',z')dS' \quad (77)$$

where $\phi^{inc}(x,z)$ represents the incident electric field (homogeneous TEM-solution), and the integral is the particular solution, i.e. the field produced by the currents on the obstacle surface. $G(x,z;x',z')$ is the Green's function defined as follows: $jkc\mu G(x,z;x',z')$ is the electric field produced at the point x',z' . $K(x',z')$ is $jkc\mu J$, where J is the surface current density on the obstacle (which is in the y-direction only).

$\phi(x,z)$ is subject to the following boundary conditions:

- i) $\partial\phi/\partial x = 0$ on the magnetic sidewalls of the model at $x = 0$ and $x = A$
- ii) $\phi = 0$ on the obstacle surface.

After separation into even and odd fields about the $z = 0$ plane, a procedure described in detail by Schwinger and Saxon¹¹ leads to the following variational expressions for the discontinuity reactances which are shown in Figure 18.

$$Z_{11} + Z_{12} = j2kA \frac{\int_{ob} K_e(x,z) G'(x,z;x',z') K_e(x',z') dS dS'}{\left[\int_{ob} K_e(x,z) \psi_e(x,z) dS \right]^2} \quad (78)$$

$$\frac{1}{Z_{11} - Z_{12}} = j2kA \frac{\int_{ob} K_o(x,z) G'(x,z;x',z') K_o(x',z') dS dS'}{\left[\int_{ob} K_o(x,z) \psi_o(x,z) dS \right]^2} \quad (79)$$

In these expressions, G' is the real part of the Green's function defined earlier. K_e and K_o are the even and odd current distribution functions on the obstacle, and ψ_e and ψ_o are the even and odd standing wave fields of the fundamental mode. $k = 2\pi/\lambda_g$, where λ_g is the wavelength of the TEM-mode on the line.

Evaluation of the Green's function $G(x, z; x', z')$

By definition, the Green's function must satisfy the inhomogeneous wave equation

$$\left(\frac{\partial^2}{\partial x^2} + \frac{\partial^2}{\partial y^2} + k^2\right) G(x, z; x', z') = \delta(x-x') \delta(z-z') \quad (80)$$

and fulfill the following conditions:

- a) $\frac{\partial G}{\partial x} = 0$ on the magnetic sidewalls of the model at $x = 0$ and $x = A$ since it is an electric field in y -direction.
- b) G must represent outgoing waves from the point x', z' since the current filaments act like sources and not like sinks.

With these conditions, the Green's function in the microstrip model becomes

$$G(x, z; x', z') = \frac{j}{2Ak} \cos k|z-z'| + G'(x, z; x', z') \quad (81)$$

where

$$G'(x, z; x', z') = \frac{j}{2Ak} \sin k|z-z'| + \frac{j}{A} \sum_{m=1}^{\infty} \frac{1}{k_m} \cos(m\pi x/A) \cos(m\pi x'/A) e^{-jk_m|z-z'|} \quad (82)$$

Expression (82) is real since only the TEM-wave was assumed to be propagating. It is to be introduced into the variational expressions (78) and (79). The wavenumber of the m -th mode is

$$k_m = (k^2 - (m\pi/A)^2)^{\frac{1}{2}}; \quad k_{(m=0)} = k \quad (83)$$

The incident wave functions in the even and odd case are respectively:

Even excitation: $\psi_e = \cos kz$ (field maximum at $z = 0$) (84)

Odd excitation: $\psi_o = \sin kz$ (field node at $z = 0$) (85)

Approximate evaluation of the variational expressions

a) Thin obstacles and windows

Since a thin obstacle or window is entirely confined to the $z = 0$ plane, the total input impedance of the bisected equivalent circuit must be equal to zero in the odd case, thus

$$Z_{11} - Z_{12} = 0 \quad Z_{11} = Z_{12} \quad (86)$$

To evaluate the even case, we choose the current density $K_e(x', z')$ to be constant over the whole obstacle surface.

$$K_e(x', z') = 1 \quad (87)$$

The denominator of eqn. (78) becomes in case of a thin centered obstacle ($\psi_e(x, z) = \cos kz = 1$ on the obstacle surface):

$$\begin{aligned} \left[\int_{\text{ob}} K_e(x, z) \psi_e(x, z) dS \right]^2 &= \left[\int_{\frac{A-d}{2}}^{\frac{A+d}{2}} 1 \cdot 1 \cdot dx \right. \\ &\quad \left. + \int_{\frac{A+d}{2}}^{\frac{A-d}{2}} 1 \cdot 1 \cdot (-dx) \right]^2 = 4d^2 \end{aligned} \quad (88)$$

Introducing the Green's function (81) and the approximate source function (87) into the numerator of eqn. (78) we obtain after integration over the whole obstacle surface and with some algebra:

$$Z_{11} + Z_{12} = 2Z = -2 \sum_{m=2}^{\text{even } m} \left(\frac{2}{m\pi} \right)^2 \left(\frac{A}{d} \right)^2 \frac{k}{k_m} \sin^2 \left(\frac{m\pi}{2} \frac{d}{A} \right) \quad (89)$$

The equivalent circuit of the obstacle is thus a shunt inductance $Z = jX$ since k_m is positive imaginary for all higher modes.

The sum in eqn. (89) converges quickly and gives good results with a few terms. In case of non-centered obstacles or windows, the limits of integration in both numerator and denominator of the variational expression (78) must be altered according to their particular geometry.

b) Cylindrical posts of circular cross-section

Again, very simple current distributions over the obstacle surface are assumed:

$$\text{Even excitation: } K_e(x', z') = 1/(2\pi R) \quad (90)$$

$$\text{Odd excitation: } K_o(x', z') = [1/(2\pi R)] \cos \theta \quad (91)$$

where R is the radius of the cylinder and θ is measured from the positive z -axis. Since two different types of co-ordinate systems, namely cartesian and cylindrical, are involved in the integration within the variational expressions, the field in the microstrip model must be represented in terms of cylindrical wave functions. (For more details see Schwinger and Saxon¹¹, p. 39 pp.) The results of the integration are:

$$Z_{11} + Z_{12} = j2 \frac{A}{\lambda_g} \left[\ln \left(\frac{A}{R} \frac{1}{2\pi \sin \frac{\pi}{A} x_o} \right) - \frac{1}{4} (kR)^2 + \sum_{m=1}^{\infty} \frac{1}{m} \left(\cos^2 \frac{m\pi x_o}{A} \right) \left(\frac{1}{m^2 - \left(\frac{kA}{\pi} \right)^2} - \frac{1}{m} \right) \right] \quad (92)$$

$$\text{and } Z_{11} - Z_{12} = -j \frac{A}{2\lambda_g} \left(\frac{2\pi R}{A} \right)^2 \quad (93)$$

where x_o is the distance of the centre of the cylindrical post from the z -axis. The theoretical expressions for the above discontinuity parameters are shown in Figures 25 and 26 and are compared with experimental data. Some improvements of the theoretical expressions are discussed in Chattopadhyay's thesis¹² and appear in these figures. It can be seen that the theory using the parallel plate model for the microstrip gives

satisfactory results at frequencies well below the cutoff frequency of the first higher mode.

The next section outlines the technique used to measure the parameters of the discontinuities which were analyzed in the present paragraph.

4. EXPERIMENTAL TECHNIQUES

In the following section, the technique of measuring the parameters of microstrip discontinuities in a resonant ring is presented. A general analysis of the resonant ring is followed by some experimental results obtained with thin transverse obstacles and cylindrical metallic posts.

A microstrip ring is defined as a microstrip transmission line which is closed in itself. All radii of curvature are large with respect to the strip width so that the fields have practically the same configuration as in a straight line of identical cross-section.

4.1. Analysis of the Resonant Ring Containing A Reciprocal Discontinuity

A microstrip ring resonates if its electrical length is an integral multiple of the guided wavelength. When a discontinuity is introduced into the ring, each resonance degenerates into two distinct modes. This splitting is conveniently interpreted in terms of even and odd excitation of the discontinuity. The even case corresponds to the incidence of two waves of equal magnitude and phase upon the discontinuity, while in the odd case, waves of equal magnitude but opposite phase are incident from both sides. Either mode of resonance can be suppressed by an appropriate choice of the point of excitation along the ring.

4.1.1 Symmetrical discontinuities

If the discontinuity is symmetrical it can be represented by a symmetrical T or π section, in one single reference plane. This plane of electrical symmetry will henceforth be called $z = 0$ plane.

As shown in Figure 18, the equivalent T-circuit of a symmetrical discontinuity can be divided into two identical half sections of zero electrical length. If the circuit is excited in the even mode, no current crosses the $z = 0$ plane. Therefore, the input impedance of each half section is not altered if the connections in this plane are cut. The normalized even input impedance at either port is thus $Z_{ie} = Z_{11} + Z_{12}$.

The normalized odd input impedance, in turn, is $Z_{io} = Z_{11} - Z_{12}$ and represents the impedance of a half-section which is short circuited in the $z = 0$ plane.

A. Lossless symmetrical discontinuities

The even and odd impedances of the discontinuity cause the shift in the resonance frequencies of the ring. This

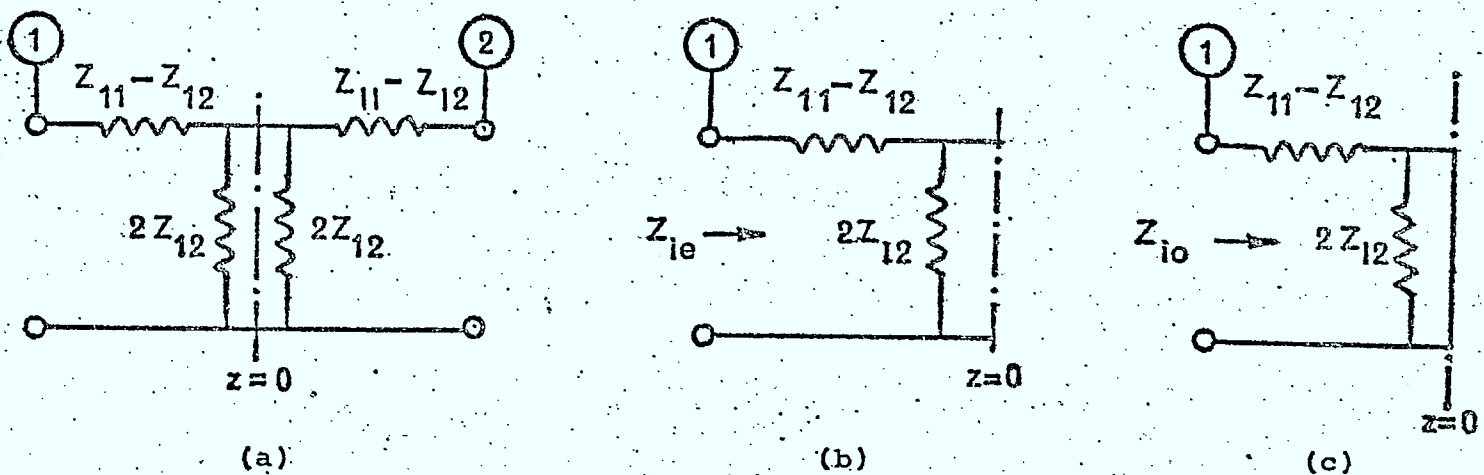


Figure 10 (a) Equivalent circuit of a symmetrical discontinuity.
 (b) One half of the equivalent circuit for even excitation.
 $Z_{ie} = Z_{11} + Z_{12}$
 (c) One half of the equivalent circuit for odd excitation.
 $Z_{io} = Z_{11} - Z_{12}$

becomes evident if the (reactive) impedances are thought of as input impedances of fictitious transmission line sections which are open (even case) or short-circuited (odd case) at the other end. (Figures 19a and 19b).

The artificial increase of the electrical length of the ring resulting in the decrease of its resonance frequencies, is related to the normalized even and odd input impedances by the following expressions:

$$Z_{ie} = Z_{11} + Z_{12} = -j \cot k \ell_e \quad (\text{even case}) \quad (1.1)$$

$$Z_{io} = Z_{11} - Z_{12} = j \tan k \ell_o \quad (\text{odd case}) \quad (1.2)$$

$k = 2\pi/\lambda_t$, is the propagation constant of the quasi-TEM mode.

Figures 20a and 20b show the standing wave pattern on the ring resonating in the fundamental mode. For convenient presentation, the ring is cut open at $z = 0$ and straightened out. The fictitious lines representing Z_{ie} and Z_{io} have been added on either side.

Since at resonance, the total electrical length of the resonator (including the discontinuity) is $n \cdot \lambda_t$, where n is the harmonic number, the resonance conditions are

$$\text{in the even case: } \ell_{\text{ring}} + 2\ell_e = n\lambda_{te} \quad (1.3)$$

$$\text{in the odd case: } \ell_{\text{ring}} + 2\ell_o = n\lambda_{to} \quad (1.4)$$

ℓ_{ring} is the physical length of the ring along the mean circumference, and λ_{te} and λ_{to} are the guided wavelengths corresponding to the even and odd resonance frequency respectively.

Since ℓ_{ring} is known and λ_t can be obtained from measurements, ℓ_e and ℓ_o are determined from equations (1.3) and (1.4).

When introduced into equations (1.1) and (1.2) respectively, they yield

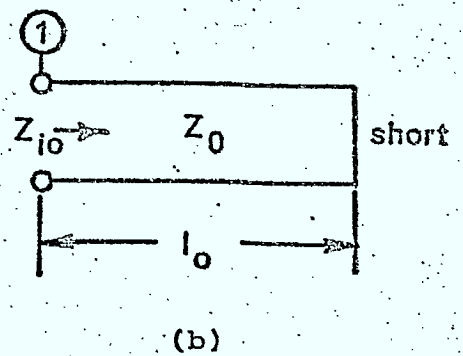
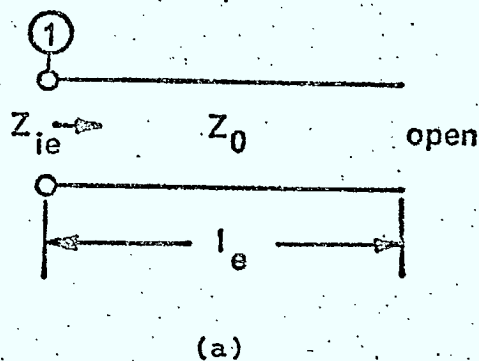


Figure 19 (a) Representation of the even input impedance Z_{ie} in plane 1 by a fictitious open-circuited line (l_e lossless discontinuity).
 (b) Representation of the odd input impedance Z_{io} in plane 1 by a fictitious short-circuited line (l_o lossless discontinuity).

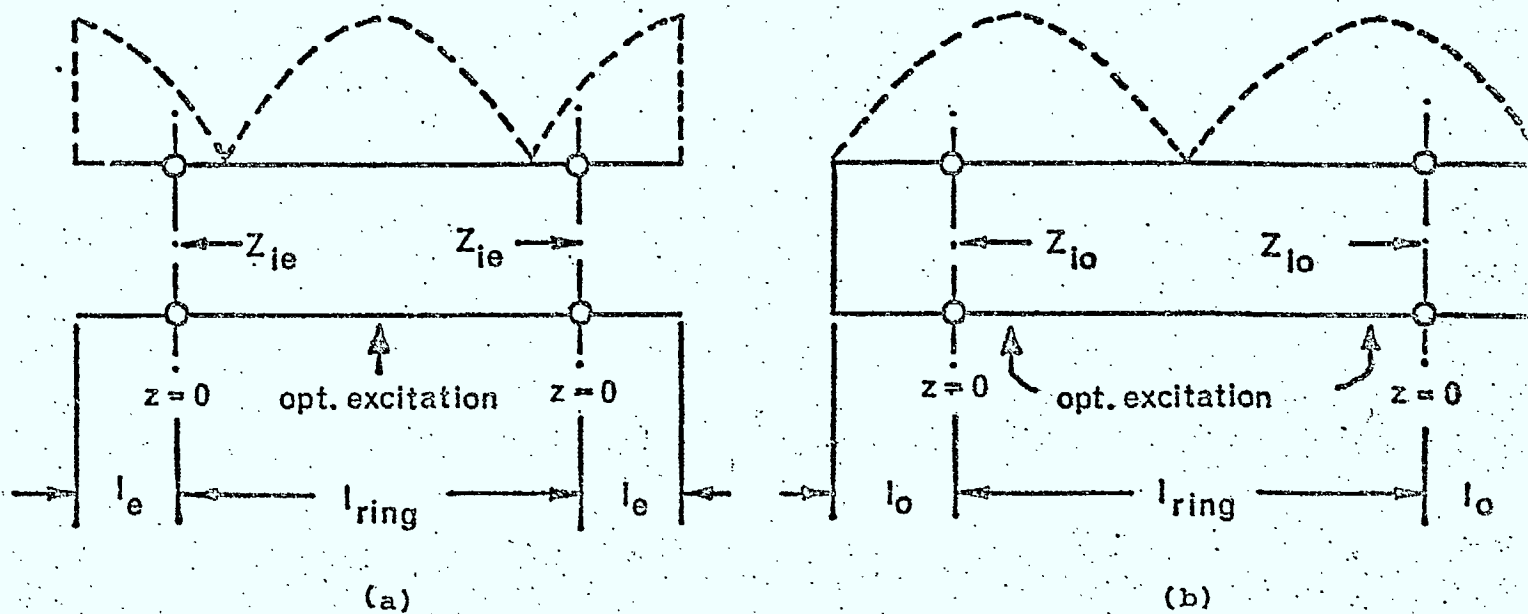


Figure 20 (a) Standing-wave pattern on the ring for even excitation of the discontinuity ($n=1$).
 (b) Standing-wave pattern on the ring for odd excitation of the discontinuity ($n=1$).

$$Z_{11} + Z_{12} = -j \cot \left[\frac{1}{2} k (n\lambda_{te} - \ell_{ring}) \right] = j \cot \left(\pi \frac{\ell_{ring}}{\lambda_{te}} \right) \quad (1.5)$$

$$Z_{11} - Z_{12} = j \tan \left[\frac{1}{2} k (n\lambda_{to} - \ell_{ring}) \right] = -j \tan \left(\pi \frac{\ell_{ring}}{\lambda_{to}} \right) \quad (1.6)$$

Since one measures resonance frequencies rather than wavelengths, it is more convenient to express λ_{te} and λ_{to} as follows:

$$\lambda_{te} = c / (f_{re} \sqrt{\epsilon_{eff}(f_{re})}) \quad (1.7)$$

$$\lambda_{to} = c / (f_{ro} \sqrt{\epsilon_{eff}(f_{ro})}) \quad (1.8)$$

and to introduce these expressions into equations (1.5) and (1.6) respectively. Thus

$$Z_{ie} = Z_{11} + Z_{12} = j \cot \frac{\pi \ell_{ring} \sqrt{\epsilon_{eff}(f_{re})} f_{re}}{c} \quad (1.9)$$

$$Z_{io} = Z_{11} - Z_{12} = -j \tan \frac{\pi \ell_{ring} \sqrt{\epsilon_{eff}(f_{ro})} f_{ro}}{c} \quad (1.10)$$

where $\epsilon_{eff}(f)$ is the dispersive effective dielectric constant of the ring, c is the speed of light, f_{re} and f_{ro} are the even and odd resonance frequencies of the perturbed ring. These expressions form the basis for the measurement technique described later on.

B. Lossy symmetrical discontinuities

Dissipation and radiation losses render the Z -parameters of discontinuities complex. The complex even and odd input impedances of the equivalent circuit can be represented by sections of transmission lines terminated in a pure resistance (Figures 21a and b).

The terminating resistance must be larger than Z_0 in the even case (voltage maximum at $z = 0$) and smaller than Z_0 in the odd case (voltage minimum at $z = 0$). Note that for the lossless case, R tends towards ∞ , while r becomes zero.

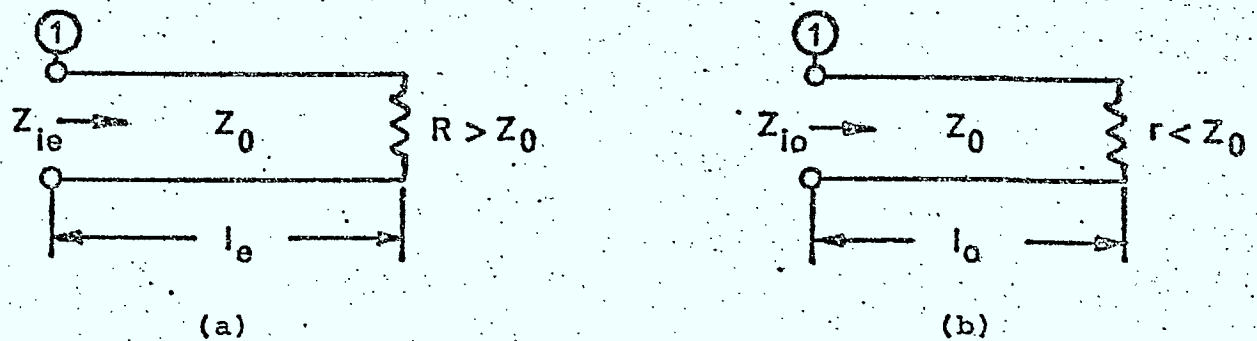


Figure 21 (a) Representation of the even input impedance Z_{ie} of a lossy discontinuity in plane 1 by a fictitious line terminated in $R > Z_0$.
 (b) Representation of the odd input impedance Z_{io} of a lossy discontinuity in plane 1 by a fictitious line terminated in $r < Z_0$.

The lengths and terminations of the fictitious lines are such that,

$$Z_{ie} = Z_{11} + Z_{12} = \frac{\frac{R}{Z_o} + j \tan k\ell_e}{1 + j \frac{R}{Z_o} \tan k\ell_e} = \frac{\frac{R}{Z_o} - j \tan \left(\frac{\pi \ell_{ring}}{\lambda_{te}} \right)}{1 - j \frac{R}{Z_o} \tan \left(\frac{\pi \ell_{ring}}{\lambda_{te}} \right)} \quad (1.11)$$

$$Z_{io} = Z_{11} - Z_{12} = \frac{\frac{r}{Z_o} + j \tan k\ell_o}{1 + j \frac{r}{Z_o} \tan k\ell_o} = \frac{\frac{r}{Z_o} - j \tan \left(\frac{\pi \ell_{ring}}{\lambda_{to}} \right)}{1 - j \frac{r}{Z_o} \tan \left(\frac{\pi \ell_{ring}}{\lambda_{to}} \right)} \quad (1.12)$$

The wavelengths λ_{te} and λ_{to} satisfy equations (1.7) and (1.8) respectively and are determined as in the lossless case. R and r affect the Q-factor of the ring.

Let Q_1 be the unloaded Q of the ring, while Q_{2e} and Q_{2o} are the loaded Q-factors of the ring for even and odd excitation of the discontinuity respectively. Then

$$\frac{R}{Z_o} = \frac{2}{\pi n} \frac{Q_1 Q_{2e}}{Q - Q_{2e}} \quad (1.13)$$

$$\frac{r}{Z_o} = \frac{\pi n}{2} \frac{Q_1 - Q_{2o}}{Q_1 Q_{2o}} \quad (1.14)$$

where n is the harmonic number.

The circuit parameters Z_{11} and Z_{12} are determined from R, λ_{te} , r and λ_{to} using equations (1.11) and (1.12).

4.1.2 Unsymmetrical discontinuities

A. Lossless unsymmetrical discontinuities

A lossless unsymmetrical discontinuity can always be transformed into a symmetrical two-port by adding an appropriate

length of line l_a to one of its ports. The plane of electrical symmetry, $z = 0$, is then situated half way between the planes with respect to which the two-port is symmetrical. Once the Z-parameters in the plane $z = 0$ are known, the impedance in any other plane can be found by simple transformation along the line.

In practice the $z = 0$ plane is easily determined since it is situated opposite to the point of optimum excitation of the ring at the fundamental even resonance.

B. Lossy unsymmetrical discontinuities

The concept of even and odd excitation can only be applied to those lossy unsymmetrical discontinuities which can be transformed into a symmetrical two port by adding an appropriate length of line to one of their ports. In terms of S-parameters, this condition is fulfilled if

$$|s_{11}| = |s_{22}|$$

The Z-parameters in the plane of electrical symmetry are then calculated using equations (1.11) and (1.12).

2. The Measurement Technique and Experimental Arrangement

4.2.1 Measurement Technique

It has been noted in section 4.1 that for making the evaluation of discontinuity parameters, measurements of resonant frequencies and Q-factors are to be done. Resonant frequencies and Q-factors of the microstrip ring change due to the introduction of a discontinuity. So, the measurements are to be done in two stages.

- i) The resonant frequencies and the unloaded Q-factors of the ring are measured before the discontinuity is introduced.
- ii) The discontinuity is then introduced (either into the same ring or, if this is impractical, into another identical ring), and the even and odd resonant frequencies together with the corresponding loaded Q-factors of the structure are measured.

The ring should be as uniform as possible since even a small irregularity may introduce effects of the same order as the effects to be measured. The ring is best excited by a capacitive launcher which can be moved along the outer contour of the ring for about one quarter of its circumference to select the optimal point of excitation for each resonance. Coupling should be as light as the sensitivity of the measuring equipment permits. Even then, the launcher changes the resonant frequencies slightly. But as long as the measurements on the empty and the perturbed ring are made at the same coupling strength, the effect of the launcher is eliminated since it affects all measurements in the same way.

Resonant frequencies can be determined from either reflection or transmission measurements. The former method has

the advantage that only one coupling link between ring and peripheral equipment is required. Care must be taken to measure all resonant frequencies with best possible accuracy since the discontinuity impedance values are very sensitive to frequency variations. This accuracy is limited by the sharpness of the resonance response rather than the performance of available counters for the microwave range.

Q-factors are best measured in the transmission mode¹³ which, unfortunately, requires a second coupling link between ring and the peripheral equipment, but may be evaluated from reflection measurements with lesser accuracy.

Changes in temperature alter the resonant frequencies of the ring. In most cases, it will be necessary to stabilize the temperature of the substrate within $\pm 0.5^{\circ}\text{C}$ if meaningful measurements are to be made.

4.2.2 Experimental Arrangement

A. The ring resonator

Measurements have been made in a ring which had the shape of a racetrack (Figure 22). The discontinuity could thus be placed into a straight section of line, and the launcher could also be moved along a straight line on the opposite side. The ring had a characteristic impedance of about 27Ω ($w/h=2.7$) on a 5 mm Stycast substrate with a nominal dielectric constant of 10.6. The mean circumference of the ring was $\ell_{\text{ring}} = 59.124$ cm for the measurements on metallic posts of circular cross-section and $\ell_{\text{ring}} = 57.375$ cm for measurements on thin metallic obstacles. The oversize substrate was chosen to minimize errors due to dimensional inaccuracies.

B. The obstacles (discontinuities)

Two types of discontinuities have been investigated, namely very thin metallic plates and cylindrical metallic posts. These were chosen because of the ease of introduction of obstacles after measurements on the empty ring were made. In both these

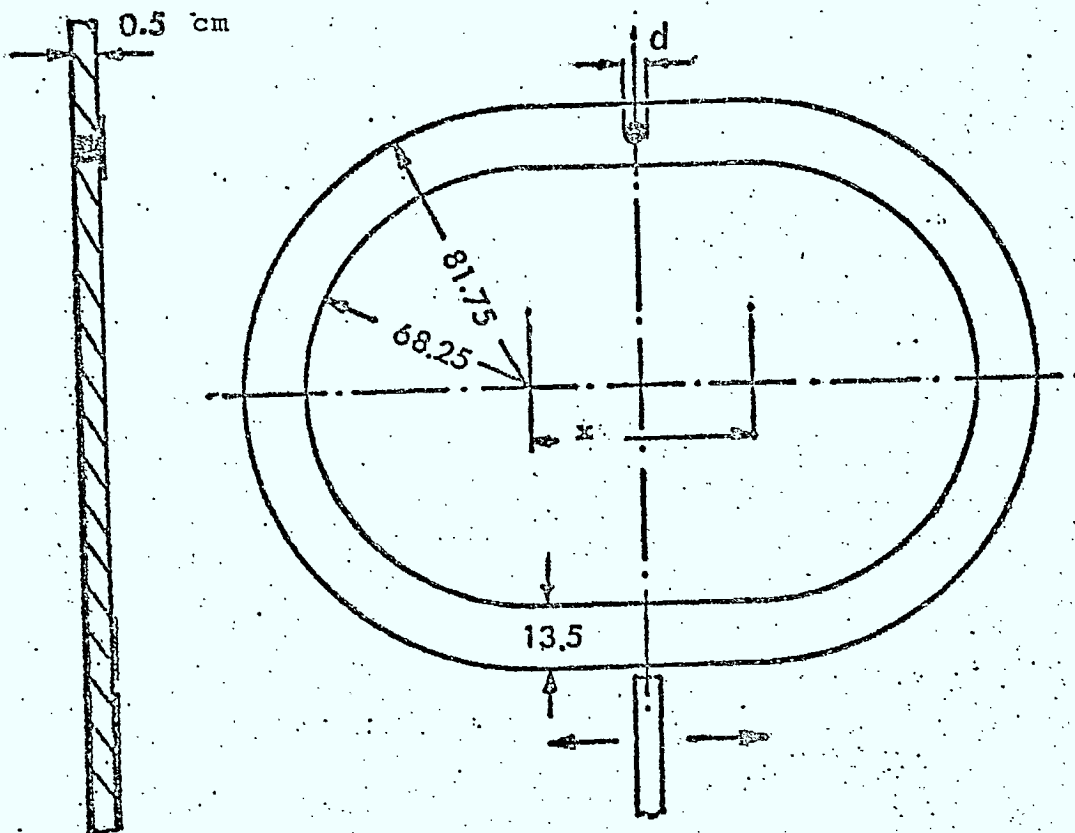


Figure 22 Microstrip ring used for measuring the Z parameters (dimensions in millimeters)

- (a) $x = 60$ mm for centered metallic posts
- (b) $x = 51.25$ mm for thin transverse obstacles.

cases, the discontinuities were centered in the cross-section of the microstrip.

The thin metallic obstacles were made of strips of very thin copper sheets. These were introduced into the ring in the following way. The ring was cut open at the intended position of the obstacle. The thin metallic foil was introduced and then the ring was reassembled. For thin obstacles, only the even resonance measurements are to be made, and for even resonances no current crosses $z = 0$ plane. Hence, cutting open of the ring does not affect the measurements.

The metallic posts were realized by drilling holes across the microstrip and filling those with mercury.

In each case, good electrical contact was insured at the strip and the ground plane, and the electrical parameters of the discontinuity could be reproduced within the limits of accuracy of the equipment.

C. The Temperature Chamber

As has been already indicated in section 4.2.1, to make the measurements of discontinuity parameters, the temperature of the substrate has to be stabilized within $\pm 0.5^\circ \text{C}$. Otherwise the dielectric constant of the substrate shows fluctuations to an extent that makes meaningful measurements impossible. For reducing the fluctuation of temperature, a temperature controlled box was designed, and the ring was placed in it.

The box as shown in Figure 23 was lined inside by a 2.5 inch thick layer of styrofoam on all sides, which is a very good temperature isolator. Only the upper lid could be removed to place the microstrip ring inside the box. A cable was introduced into the box through a very small hole in one side of the box, and that served as the connection between the

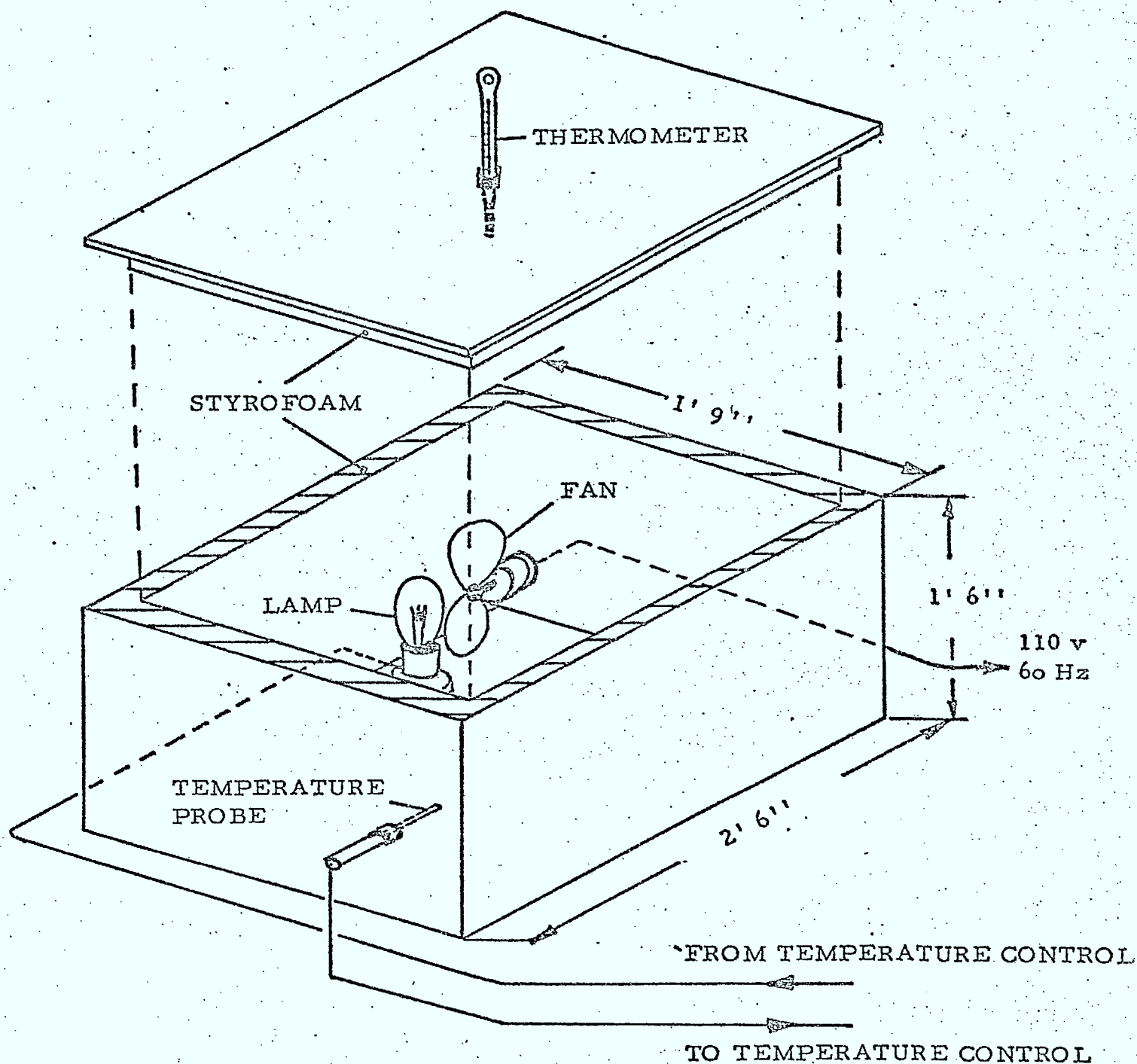


Figure 23 Temperature controlled box used for the stabilization of the temperature of the substrate.

launcher for the ring and the peripheral equipment. By pulling or pushing the cable from outside, the launcher could be placed at the appropriate excitation points along the ring. A temperature probe and a heater element, connected to a temperature control equipment outside, was also mounted within the box. During the course of the experiments, the temperature control equipment was set at 30.5°C . The sensitivity of the equipment permitted the temperature within the box to be kept in the range $30.5^{\circ}\text{C} \pm 0.4^{\circ}\text{C}$. To insure that the whole temperature chamber was being heated uniformly, a small fan circulated the air in the box continuously. The temperature inside the box was constantly monitored with the help of a thermometer which was introduced through a very small hole in the top lid of the box.

D. The Measurement Procedure

The circuit for the measurement of the resonance frequencies was laid out as shown in Figure 24. The reflection characteristics of the resonant ring were measured using a network analyzer. The ring response was observed on a phase-magnitude display. A spectrum analyzer was used to compare the resonance frequencies of the ring with the frequency of a precision frequency generator. The output frequency of the generator was displayed on a digital frequency counter. The vertical output of the spectrum analyzer was fed to the network analyzer as the z-axis marker.

Now we shall describe the procedure followed to determine exactly any particular resonance frequency. To start with, the sweep oscillator was sweeping in Δf mode. By changing the central frequency of the sweep, the response of the ring was centered on the screen of the phase-magnitude display. Then the sweep was changed to manual and the output frequency of the sweep oscillator was set as close to the peak as possible. Now the local oscillator of the spectrum analyzer was adjusted and tuned such that the sweep oscillator

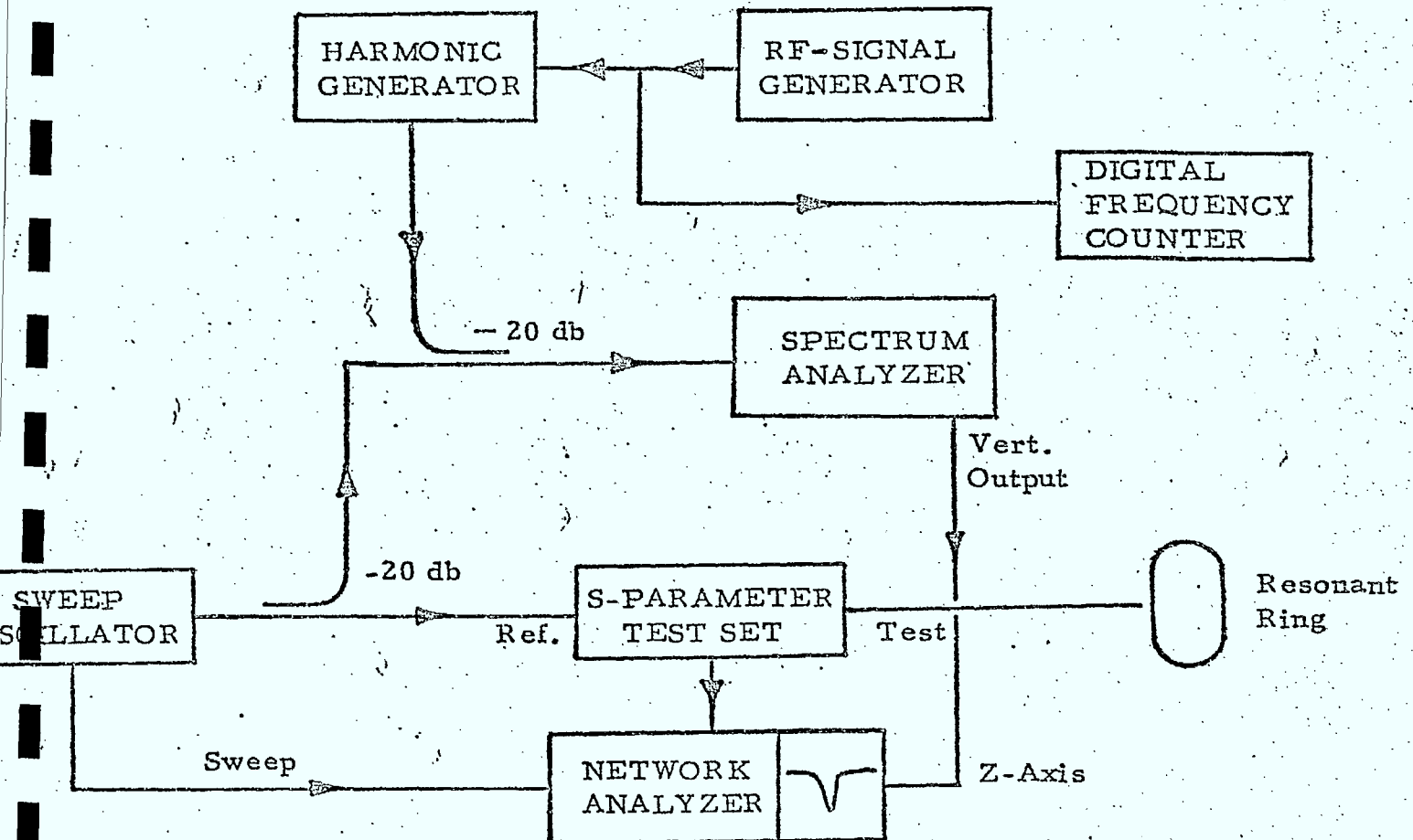


Figure 24 Circuit diagram for measuring the resonance frequencies of the microstrip ring.

frequency was in the centre of the spectrum analyzer screen. Then the scanning mode of the spectrum analyzer was changed to "manual". The sweeper was again swept in automatic mode at a very low speed. The vertical output of the spectrum analyzer density modulated the phase-magnitude display, producing a dot on the absorption curve very near to its peak. The frequency of the spectrum analyzer was now finally adjusted to place the dot exactly on the peak. Now the frequency of the r.f. signal generator output was adjusted. As soon as this frequency became identical with the centre frequency of the spectrum analyzer (which in turn was tuned to the ring resonant frequency), the intensity of the phase-magnitude display trace increase drastically over the whole sweeping range. Under this setting, the frequency of the r.f. signal generator output is the required resonance frequency of the ring.

The r.f. signal generator available for our experiments had a frequency range much smaller than the range (.1-2GHz) over which the ring resonances were being studied. This difficulty was avoided by inserting a harmonic generator unit between the r.f. signal generator and the spectrum analyzer. By properly choosing r.f. frequency and using its proper harmonics it was always possible to match any ring resonance frequency.

Measurements of frequencies of the peaks of absorption could be repeated within ± 20 KHz.

E. Some Experimental Results

Results of measurements made on metallic posts and thin obstacles are presented in Figures 25 and 26. For comparison, theoretical values which have been obtained using the variational principle, are shown concurrently. Both experiment and theory agree quite well for low frequencies.

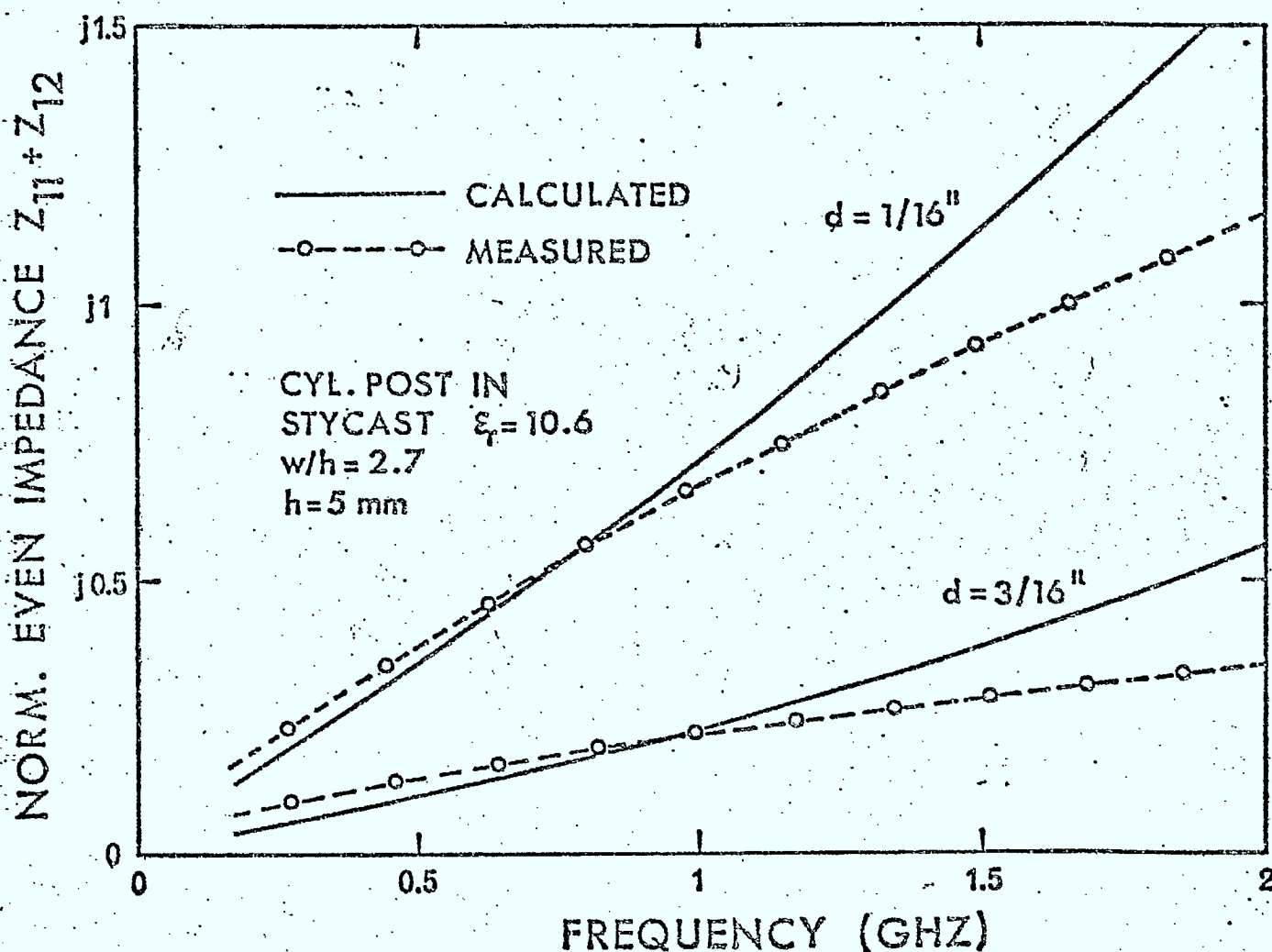


Figure 25 (a). Normalized even impedances of centered metallic posts of circular cross-section in a 27Ω line on Stycast ($\epsilon_r = 10.6$; $h = 5 \text{ mm}$; $w/h = 2.7$). Post diameter $d = 1/16 \text{ in.}$, post diameter $d = 3/16 \text{ in.}$

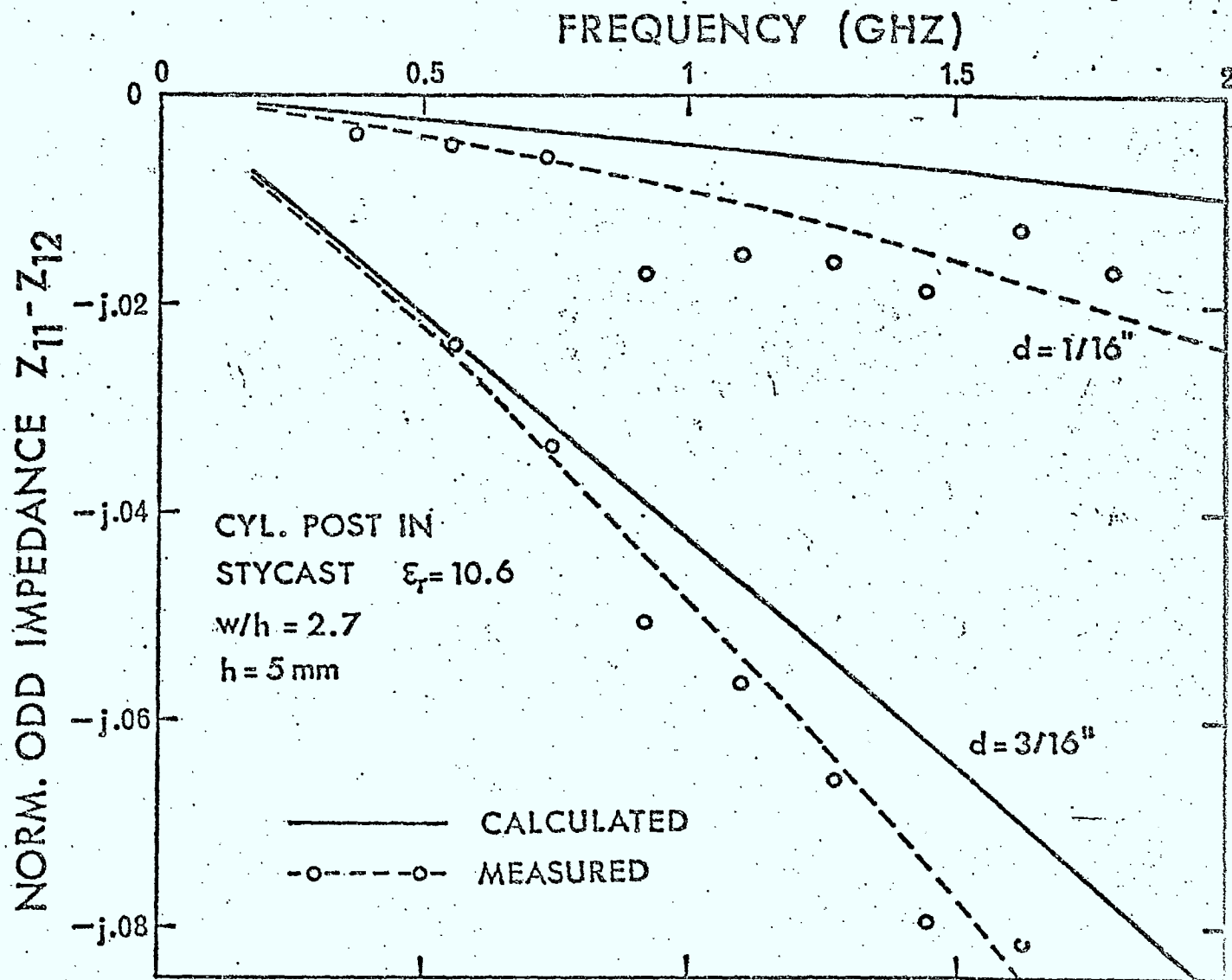


Figure 25 (b). Normalized odd impedances of centered metallic posts of circular cross-section in a 27Ω line on Stycast ($\epsilon_r = 10.6$; $h = 5 \text{ mm}$; $w/h = 2.7$). Post diameter $d = 1/16 \text{ in.}$ post diameter $d = 3/16 \text{ in.}$

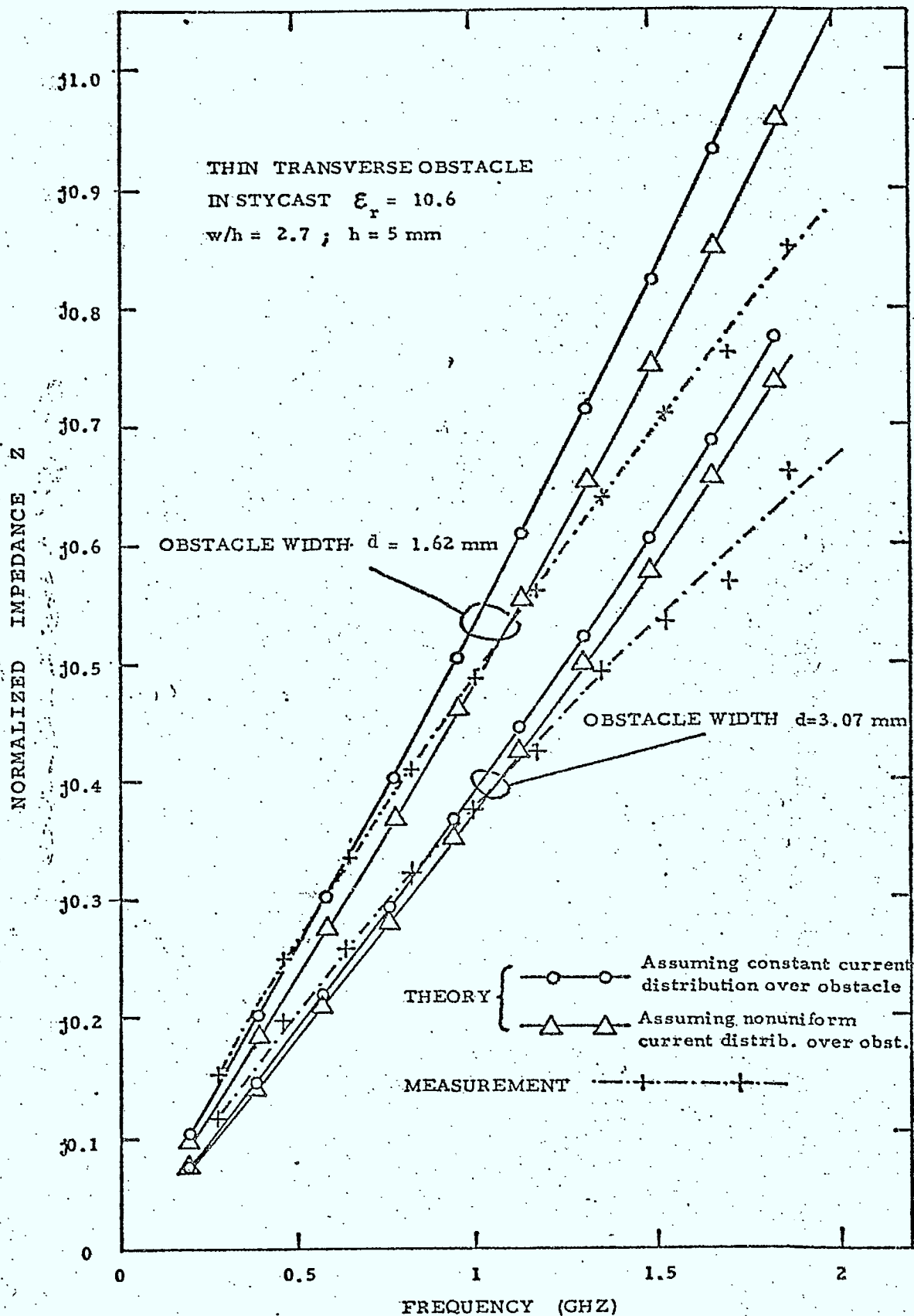


Figure 26. Normalized impedance of thin transverse obstacle in a 27Ω line on Stycast ($\epsilon_r = 10.6$; $h = 5$ mm; $w/h = 2.7$). Obstacle width $d = 1.62$ mm; obstacle width $d = 3.07$ mm.

3. Error Analysis for Experimental Characterization of Lossless Discontinuities in Resonant Rings

A general study of the resonant ring method for the characterization of microstrip discontinuities have been given in section 4.1. In the present chapter we will analyze the accuracy with which the equivalent circuit parameters of reciprocal lossless discontinuities can be measured in resonant rings [3].

Let us recall from section 4.1 (equations (1.9) and (1.10)) that the normalized even and odd mode input impedances at either port of the equivalent circuit of Figure 22 can be given as

$$Z_{ie} = Z_{11} + Z_{12} = j \cot \left(\frac{\pi l_{\text{ring}} \sqrt{\epsilon_{\text{eff}}(f_{re})} f_{re}}{c} \right) \quad (3.1)$$

$$Z_{io} = Z_{11} - Z_{12} = -j \tan \left(\frac{\pi l_{\text{ring}} \sqrt{\epsilon_{\text{eff}}(f_{ro})} f_{ro}}{c} \right) \quad (3.2)$$

where l_{ring} is the physical mean length of the ring, ϵ_{eff} is the effective dispersive dielectric constant of the line at the resonance frequencies of the loaded ring for even (f_{re}) and odd (f_{ro}) excitation of the discontinuity, and c is the velocity of light.

Moreover, as has been seen in section 4.2 the measurement of the parameters of a lossless discontinuity is performed in two stages:

- i) The resonant frequencies of the ring are measured before the discontinuity is introduced. They yield the dispersive permittivity ϵ_{eff} of the line.
- ii) The discontinuity is then introduced and the degenerated even and odd resonance frequencies of the structure are measured. Since these frequencies

are in general different from those measured in 1), the values of ϵ_{eff} that are used in equations (3.1) and (3.2) must be found by interpolation.

When the systematic errors due to dimensional inaccuracies of the resonant ring are practically eliminated, the accuracy of the measured discontinuity impedances depends on the accuracy with which the frequency of the resonance peaks can be located and measured.

Let us first consider how the even discontinuity impedance Z_{ie} is susceptible to the errors in frequency measurements. Since the error in the measurement of Z_{ie} depends on the error with which both empty and loaded ring resonance frequencies are determined, we can write

$$dZ_{ie} = \frac{\partial Z_{ie}}{\partial f_e} df_e + \frac{\partial Z_{ie}}{\partial f_{re}} df_{re} \quad (3.3)$$

where f_e denotes the resonance frequency of the empty ring. We shall evaluate the two terms of equation (3.3) separately.

Z_{ie} is dependent on the empty resonance frequency implicitly through ϵ_{eff} . So, we can write

$$\frac{\partial Z_{ie}}{\partial f_e} = \frac{\partial Z_{ie}}{\partial (\sqrt{\epsilon_{\text{eff}}})} \frac{\partial (\sqrt{\epsilon_{\text{eff}}})}{\partial f_e} \quad (3.4)$$

using equation (3.1),

$$\frac{\partial Z_{ie}}{\partial \epsilon_{\text{eff}}} = -j \frac{\pi l_{\text{ring}} f_{re}}{c} \cdot \frac{1}{\sin^2 \left(\frac{\pi l_{\text{ring}} \sqrt{\epsilon_{\text{eff}}} f_{re}}{c} \right)} \quad (3.5)$$

Now,

$$\frac{1}{\sin^2 \left(\frac{\pi l_{\text{ring}} \sqrt{\epsilon_{\text{eff}}} f_{re}}{c} \right)} = 1 + \cot^2 \left(\frac{\pi l_{\text{ring}} \sqrt{\epsilon_{\text{eff}}} f_{re}}{c} \right) \quad (3.6)$$

$$= 1 + Z_{ie} Z_{ie}^* \quad (\text{by equation (3.1)}) \quad (3.7)$$

$$= 1 + |Z_{ie}|^2 \quad (3.8)$$

Therefore,

$$\frac{\partial Z_{ie}}{\partial (\sqrt{\epsilon_{eff}})} = -j (1 + |Z_{ie}|^2) \frac{\pi l_{ring} f_{re}}{c} \quad (3.9)$$

Again,

$$\frac{\partial (\sqrt{\epsilon_{eff}})}{\partial f_e} = -\frac{nc}{l_{ring}} \cdot \frac{1}{f_e^2} \left[\dots \sqrt{\epsilon_{eff}} = \frac{nc}{l_{ring} f_e} \right] \quad (3.10)$$

$$= -\frac{\sqrt{\epsilon_{eff}}}{f_e} \quad (3.11)$$

So, using equations (3.4), (3.9) and (3.11)

$$\frac{\partial Z_{ie}}{\partial f_e} = j (1 + |Z_{ie}|^2) \frac{\pi l_{ring} \sqrt{\epsilon_{eff}}}{c} \cdot \frac{f_{re}}{f_e} \quad (3.12)$$

Now, let us see the dependence of Z_{ie} on f_{re} . In equation (3.1) f_{re} appears both explicitly and implicitly (due to the presence of ϵ_{eff}). Since ϵ_{eff} increases linearly with frequency, we may write

$$\epsilon_{eff}(f_{re}) = \epsilon_1 + b f_{re} \quad (3.13)$$

where ϵ_1 = effective permittivity at zero frequency
and $b = d\epsilon_{eff}/df = \text{slope of } \epsilon_{eff} \text{ vs frequency plot.}$

Using this we obtain,

$$\frac{\partial Z_{ie}}{\partial f_{re}} = -j (1 + |Z_{ie}|^2) \frac{\pi l_{ring}}{c} \left[\frac{b f_{re}}{2\sqrt{\epsilon_1 + b f_{re}}} + \sqrt{\epsilon_1 + b f_{re}} \right] \quad (3.14)$$

$$= -j (1 + |Z_{ie}|^2) \frac{\pi l_{ring}}{c} \left[\frac{3\epsilon_{eff} - \epsilon_1}{2\sqrt{\epsilon_{eff}}} \right] \quad (3.15)$$

Hence combining equations (3.3), (3.12) and (3.15) we get,

$$\frac{dz_{ie}}{z_{ie}} = j \frac{(1+|z_{ie}|^2)}{z_{ie}} \cdot \frac{\pi \ell_{ring}}{c} \cdot \left[\sqrt{\epsilon_{eff}} \frac{f_{re}}{f_e} df_e + \frac{\epsilon_{eff}^{1-3\epsilon_{eff}}}{\sqrt{\epsilon_{eff}}} df_{re} \right] \quad (3.16)$$

Proceeding in a similar way for z_{io} we get exactly the same expression for dz_{io}/z_{io} .

Under the conditions that

(a) even and odd resonance frequencies are very close to empty resonance frequencies.

and (b) $bf/\epsilon_1 \ll 1$ (where f = either f_{re} or f_{ro}), both of which hold in practice, the expression for the relative error in the measurement of even as well as odd discontinuity impedance simplifies to

$$\frac{dz_i}{z_i} = j \frac{(1+|z_i|^2)}{z_i} \cdot \frac{\pi \ell_{ring} \sqrt{\epsilon_{eff}}}{c} (df_e - df_r) \quad (3.17)$$

where df_e and df_r denote the absolute errors committed in the measurement of empty and loaded ring frequencies respectively. These errors reflect the precision with which the resonance frequencies of the ring can be located. It is not so much determined by the accuracy of the frequency counter as by the sharpness of the observed resonance peaks. A good estimate of df_e and df_r can be obtained by measuring several times the resonance frequencies and finding the standard deviation of the results from their calculated average.

Table 2 presents the relative error in discontinuity impedance as a function of absolute impedance values for several standard deviations for the worst case where $df_e = df_r$. The same results are presented graphically in Figure 27.

From equation (3.17) and Figure 27 we can conclude the following:

TABLE 2

Relative Error in (Normalized) Discontinuity Impedance as a
Function of Absolute (Normalized) Impedance.

(Stycast Ring, $\ell_{\text{ring}} = 59.124 \text{ cm}$, $\epsilon_{\text{eff}} = 7.60$)

Z_i (Normalized)	dZ_i/Z_i (normalized) in % for $df_e = -df_r =$			
	30Kz	40Kz	50KHz	60KHz
1	0.205	0.273	0.342	0.410
.1	1.035	1.380	1.725	2.070
.01	10.249	13.666	17.082	20.499
.001	102.483	136.644	170.805	204.966

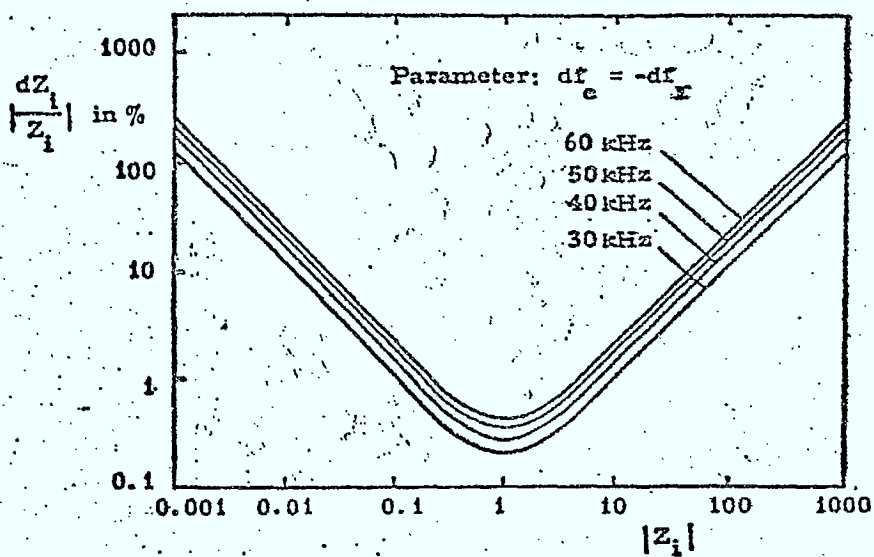


Figure 27. Relative error in discontinuity impedance vs. absolute impedance for several values of resolution in frequency measurements.
($\epsilon_{err} = 7.6$, $l_{ring} = 59.124$ cm)

- 1) The accuracy of the discontinuity impedance values is directly proportional to the accuracy with which the resonance frequencies can be located and measured.
- 2) For a given accuracy in frequency measurements, the obtained impedance value is most accurate if the absolute value of the normalized impedance is close to unity.
- 3) All errors affecting the measurement of f_e and f_r in the same way have practically no effect on the accuracy of Z_1 . Thus the influence of the capacitive launcher on the measurement of the discontinuity impedances can be neglected as long as the coupling gap is the same for all measurements.

5. CONCLUSION

In this report, several selected MIC-structures have been analysed using models with magnetic sidewalls for the open planar configurations. The reason for this was to create reasonable boundary conditions in order to make closed form solutions for these problems possible. As a result, simple formulae have been obtained for the external loading factor of cavities and triangular planar resonators coupled to microstrip and waveguide in several ways, and for equivalent circuit parameters of some transverse microstrip discontinuities. Hole coupling between cavities and microstrip as well as scattering on microstrip discontinuities has been verified experimentally, and good agreement has been observed between theory and measurement for a wide range of parameters. When necessary, corrective expressions have been derived to better describe the physical situation in extreme cases in order to ensure that the theoretical formulae are appropriate for design over a maximum range of system parameters.

6. REFERENCES

- 1 Wheeler, H. - Transmission line properties of parallel strips separated by a dielectric sheet, IEEE Trans. on Microwave Theory and Techniques, Vol. MTT-13, March 1965, pp. 172-185.
- 2 Getsinger, W.J. - Microstrip Dispersion Model, IEEE Trans. on Microwave Theory and Techniques, Vol. MTT-21, January 1973, pp. 34-39.
- 3 Wolff, I.; Kompa, G.; Mehran, R. - Streifenleitungs diskontinuitaeten und - Verzweigungen, Nachrichten technische Zeitschrift NTZ, Vol. 25, No. 5, Mai 1972, pp. 217-264.
- 4 Schelkunoff, S.A. - Electromagnetic Waves, Chapter 10, pp. 393-397, D. Van Nostrand Company, 1945.
- 5 Akaiwa, Y. - Operation Modes of a Waveguide Y Circulator, IEEE Trans. on Microwave Theory and Techniques, Nov. 74, pp. 954-960.
- 6 Wheeler, H. - Coupling holes between resonant cavities or waveguides evaluated in terms of volume ratios, IEEE Transactions on Microwave Theory and Techniques, Vol. MTT-12, March 1964, pp. 231-244.
- 7 Hoefer, W.J.R.; James D.S. - Microstrip to Waveguide Coupling through Holes, Proc. of the 5th Colloquium on Microwave Communication, Budapest, 24-30 June, 1974, MT-221 to 231.
- 8 Groebner, W., Hofreiter, N. - Integraltafel - Zweiter Teil: Bestimmte Integrale - Springer Verlag, Wien und Innsbruck, 1950, p. 189.

- 9 Bethe, H.A. - Theory of diffraction by small holes,
 Phys. Review, Vol. 66, Oct. 1944, pp. 163-182.
- 10 Montgomery, C.G. et al. - Principles of Microwave
 Circuits, Boston Technical Publishers, 1964, p. 178.
- 11 Schwinger, J.; Saxon, D.S. - Discontinuities in
 Waveguides, Gordon and Breach Science Publishers,
 New York, 1968.
- 12 Chattopadhyay, A. - A contribution to theoretical
 and experimental characterization of microstrip
 discontinuities, Ph.D.-Thesis, Dept. of El. Engineering,
 University of Ottawa, February 1976.
- 13 Hoefer, W.J.R.; Painchaud, G.R. - Frequency markers
 providing resolution of 1 kHz for swept microwave
 measurements, Electronics Letters, Vol. 10, pp. 123-124,
 April 1974.
- 14 Chattopadhyay, A.; Hoefer, W.J.R. - Error analysis
 for characterization of microstrip discontinuities in
 resonant ring, - Intl. Electrical, Electronics Conf.
 and Exposition, Sept. 1975, Toronto, Canada.
- 15 Hoefer, W.J.R.; Chattopadhyay, A. - Evaluation of
 the equivalent circuit parameters of microstrip
 discontinuities through perturbation of a resonant
 ring, IEEE Trans. on Microwave Theory and Techniques,
 Vol. MTT-23, No. 12, Dec. 1975, pp. 1067-1071.

LKC

P91 .C654 H63 1976

Analytical approach to the
design of selected microwave of
integrated circuit it
structures : final report

P
91
C654
H641
1976

DATE DUE
DATE DE RETOUR

02. MAY 03

LOWE-MARTIN No. 1137

INDUSTRY CANADA / INDUSTRIE CANADA



208113

